IEEE Access
Multidisciplinary | Rapid Review | Open Access Journal

SPECIAL SECTION ON BIG DATA LEARNING AND DISCOVERY

Received November 13, 2018, accepted December 27, 2018, date of publication January 31, 2019, date of current version February 20, 2019.

Digital Object Identifier 10.1109/ACCESS.2019.2894715

POD-Based Data Mining of Turbulent Flows in Front of and on Top of Smooth and Roughness-Resolved Forward-Facing Steps

YANG SHAOQIONG[1,2,3], WANG YANHUI[1,2], YANG MING[1], SONG YANG[1], AND WU YANHUA[3]

[1]School of Mechanical Engineering, Tianjin University, Tianjin 300352, China
[2]Qingdao National Laboratory for Marine Science and Technology (QNLM), Qingdao 266237, China
[3]School of Mechanical and Aerospace Engineering, Nanyang Technological University (NTU), Singapore 639805

Corresponding authors: Yang Shaoqiong (shaoqiongy@tju.edu.cn) and Wu Yanhua (yanhuawu@ntu.edu.sg)

This work was supported in part by the National Key R&D Program of China under Grant 2016YFC0301101 and Grant 2017YFC0305902, in part by the Natural Science Foundation of Tianjin City under Grant 18JCQNJC05100, in part by the Key R&D Program of Shandong under Grant 2016CYJS02A02, in part by the Aoshan Talents Program of QNLM in China under Grant 2017ASTCP-OS05 and Grant 2017ASTCP-OE01, and in part by the Ministry of Education, Singapore, under Grant RG 52/11 and Grant ARC 3/15.

ABSTRACT A new application of proper orthogonal decomposition (POD) to uncover the relation of the instantaneous energetic large-scale turbulent structures to the dominant POD modes had been reported. Motivated on this method, the data mining from the velocity vector fields measured by the particle image velocimetry and structural analysis on the selected POD-based reconstructed turbulent flows in front of and on top of smooth and roughness-resolved forward-facing steps (FFSs) has been performed. The velocity fields containing the most energetic large-scale structures are conditionally chosen. The conditional criterion is that the chosen velocity fields whose POD temporal coefficients of the first or second mode are correspondingly larger than twice of their root mean square values. Typically, the most energetic instantaneous structures are the large-scale second-quadrant (Q2) or fourth-quadrant (Q4) events and the mostly open separation bubbles in front of these FFSs; while the large-scale structures behave as a strong shear layer, and near or in which are a few spanwise prograde or retrograde vortices; and sometimes the alternating node and saddle points appeared. Similarly, for the flow on top of the FFSs, the most energetic structures are presented as a great many large-scale Q4 or Q2 events and a few secondary vortices at the very near wall; while the large-scale structures are overall exhibited as a strong shear layer, and in which a large number of vertex structures are created. These energetic large-scale structures here are not only sensitive to the surface roughness conditions but also to the spanwise locations.

INDEX TERMS Proper orthogonal decomposition, data mining, PIV, turbulent flow, forward-facing step, reconstructed flow structure, surface roughness.

I. INTRODUCTION

A. FORWARD-FACING STEP FLOWS

The turbulent flow through a forward-facing step (FFS) has been studied for several decades due to their separating and reattaching flow phenomena which may lead to flow-induced noises and structural vibrations in many industrial and engineering applications such as the heat transfer enhancement or cooling for the electronic devices etc. The canonical smooth FFS flows can be divided into three distinct regions, *i.e.*, (I) an upstream recirculation region in front of the step due to an adverse pressure gradient locally incurred by the FFS blockage; (II) a primary recirculation region on top of the upstream FFS where the flow is separated by the sharp leading edge of the step, and note that a strong shear layer, similar to a mixing layer, between the low-velocity reverse flow and the mean free stream flow, develops above the downstream recirculation region; and (III) a redevelopment region after the flow being reattached (*cf.* [1, Fig. 1]). In Region I, the turbulent flow was separated at the wall upstream about 0.8-1.5h ahead of the FFSs; and to reattach on the vertical wall of the step at approximately 0.6-0.7h where h is the height of step [2], [3]. Pearson *et al.* [4] also reported that the turbulent separation bubbles in this region exhibited both open and closed forms for equally

approximately half of the time by conditional averaging based on the area of reverse flow. For Region II, Sherry *et al.* [1] (*cf.* Table 1) summarized the past studies of the statistics characteristics for the turbulent flows on top of the smooth FFSs, which are affected by the incoming flow or geometry parameters such as the height ratio between the upstream boundary layer and the step δ/h, step length aspect ratio L/h and Reynolds number Re_h. The authors concluded that the mean reattachment length X_r (the distance between the leading edge of the step and the reattachment point) increased monotonically with Re_h for a given δ/h ratio. Furthermore, Largeau and Moriniere [3] believed that the external turbulence ratio u'^2/U^2 affects the development of this downstream recirculation bubble structure as well. Also, considering the practical applications in industry and engineering where the steps are usually roughness-resolved, Wu and Ren [5] and Rifat *et al.* [6] investigated the effects of realistic resolved-roughness on the FFS flows. Their results reveal that the statistical characteristics of the turbulent flows through the FFSs such as streamwise mean velocity, mean Reynolds stresses and turbulent kinetic energy (TKE) are sensitive to the different surface conditions for the roughness levels of FFSs. However, as introduced above, past studies were mainly focused on the statistical characteristics of either the smooth or roughness-resolved FFSs flows. To our knowledge, few studies have been performed to illustrate the instantaneous turbulent fluctuating structures in front of and on top of the smooth or roughness-resolved FFSs by data mining method. Largeau and Moriniere [3] have reported those structures behaving like different shapes in three regions. They are horseshoe-like bubble structures at upstream of Region I; several saddle and nodal points corresponding to the small branched structures in front of steps and flapping motions of the shear layer in Region II, and secondary structures developing within the recirculation bubble at the downstream of Region II. Lastly, they shed downstream into Region III (cf. [3, Fig. 5]). These kinds of flow structures, the most energetic and large-scale ones, in particular, are closely linked with the generation of flow-induced noise and structural vibrations. Therefore, to make a structural analysis on and then to control them in these kinds of turbulent flows through the smooth FFSs and the one with different roughness resolution might be of benefit for engineering applications.

B. PROPER ORTHOGONAL DECOMPOSITION

Lumley [7] pioneered the use of Proper orthogonal decomposition (POD) to study the internal structures in inhomogeneous turbulence. Since that time, the method of POD has become one of the data mining tools to do the structural analysis on generic turbulent flows [8]. Tang and Jiang [9] apply the POD method to study hairpin-like vortices generated by a hemisphere protuberance for comparison with the dynamic mode decomposition (DMD) method. They believed that POD concentrates on a representation in the spatial orthogonality way while the DMD algorithm focuses on a representation based on the temporal orthogonality. Feng *et al.* [10] performed a POD analysis of vortex dynamics of a circular cylinder under their synthetic jet control, presenting the variations of the POD energy, mode, coefficient and the reconstructed spanwise vorticity. Zhang *et al.* [11] conducted a comprehensive comparison on the identification of multi-dominant vortical structures in the real wake flows behind a single cylinder and two side-by-side cylinders of different diameters by applying the POD and DMD algorithms into their high-repetition time-resolved particle image velocimetry (TR-PIV) data. Besides, Zhang and Liu [12] used POD to efficiently extract the energetic coherent structures by spatially filtering the small-scale background noise from their planar PIV data of the separated shear layers around finite blunt plates. Actually, since the year 2000, the POD filtering function has already been concluded as a very effective scale-decomposition in inhomogeneous turbulent flows [13]. Furthermore, Wang *et al.* [14] recently proposed a new method named POD-OC for post-processing to reconstruct an instantaneous velocity field using the low-order high-energy POD modes. Very recently, Shao and Agelin-Chaab [15] reported their POD investigation results about the effects of different surface conditions on turbulent flows over the FFSs. The authors concluded that the different roughness of FFSs affected even the large-scale structures but did not affect the most energetic structures in the first POD mode. However, the physical mechanisms involved in it are still unknown as their POD mode-shapes are not real vortices although they are associated with the coherent structures in the flows [16]. Recently, in particular, Wu (2014) devised a new application of the POD to reveal the relationships between the first two dominate POD modes and the instantaneous energetic large-scale structures in turbulent boundary layers (TBLs). Based on this method, the present work aims to perform a comparative structural analysis on the conditional-chosen instantaneous flow fields and the selected POD-based reconstructed turbulent flows in front of and on top of the smooth and roughness-resolved FFSs. It will give more useful information about the separated and reattached flows, which thereby helps to control these energetic large-scale structures in such kind of flows over the FFSs due to their diverse industrial and engineering applications.

Since the principle and its equations of POD have been introduced by Lumley [7] and reviewed by Berkooz *et al.* [8] and they can also be found in the references above, we only briefly summarized the POD procedures herein for better understanding it. In the present study, the snapshot POD [17] is applied to mode-decompose the PIV-measured velocity vector fields (subtracting the ensemble average at first) of the turbulent flows in front of and on top of the smooth and roughness-resolved FFSs. In the two-dimensional (2D) POD, any instantaneous velocity fluctuation in the streamwise-wall-normal (x-y) plane, $u'(x, y, t)$, can be decomposed into the

TABLE 1. Experimental parameters.

U_∞(m/s)	u_τ(m/s)	δ(mm)	h(mm)	ν ($\times 10^{-5}$ m^2/s)	Re_h	δ/h	L/h	W/h	h/H
8.4	0.309	50.8	6.35	1.54	3450	8	14.2	26.6	0.01

form of

$$u'(x, y, t) = \sum_{n=1}^{N} a_n(t)\Phi_n(x, y), \quad (1)$$

where x, y are coordinates; t indicates either time-dependent or time-independent snapshots of the whole the PIV measured velocity fields; and $\Phi_n(x, y)$ is the n-th mode of POD with total spatial modes of N. $a_n(t)$ are their corresponding POD temporal coefficients which can be firstly calculated by solving the eigenvalue or eigenvector problem with a positive definite Hermitian kernel of the form

$$\lambda_n a_n(t) = \int_T (\int_\Omega u'(x, y, t)u'(x, y, t')dxdy)a_n(t')dt', \quad (2)$$

where the integrations are over the spatial domain Ω and a time interval T. For an ensemble of measured velocity fields, Ω could be the whole or part of the field of view (FOV) while T represents the ensemble or the collection of the velocity field samples. The eigenvalues λ_n are real and positive; and form a decreasing and convergent series [18], [19]. Then, the POD modes can be computed through the equation

$$\Phi_n(x, y) = \frac{\int_T u'(x, y)a_n(t)dt}{\int_T [a_n(t)]^2 dt}, \quad (3)$$

and the eigenvalues $\lambda_n = \int_T [a_n(t)]^2 dt$ as the POD is always normalized to be orthonormal. This indicates that the larger value of $[a_n(t)]^2$, the more contribution to λ_n. As concluded by Wu [18], the important temporal coefficients $a_n(t)$ of POD, either the positive or negative one both contain equivalently important information on the major contributing flow structures to the n-th POD mode, which can be used to identify the instantaneous fluctuating flow structures that contribute significantly to the first few low-order dominant POD modes.

Lastly, the TKE is equal to half of the summation of the eigenvalues' squares, *i.e.*, $\frac{1}{2}\sum_{n=1}^{N}\lambda_n^2$. Besides, as previously mentioned, for filtering the PIV measurement errors, a sufficient number of modes with about 90% of TKE will be used to reconstruct the flow fields for comparison study with the original velocity fields since flow structures observed in a single mode do not necessarily correspond to real physical flow patterns except that it has very high energy in a single snapshot, or the structure is identical in many cycles [20].

II. EXPERIMENTS

As this study focuses on the data analysis with POD method, only the necessary experimental information is briefly recalled and summarized in Table 1 for easy reading. Moreover, more details of experimental set-up can be founded in Ren and Wu [2] and Wu and Ren [5]. The 2D PIV experiments were conducted in a boundary layer wind tunnel (free-stream turbulence intensity ∼0.45%) whose test section is $0.67\times0.67\times3$ m^3 (width × height (H) × length). The boundary layer is tripped by a diameter-4.7mm cylindrical rod, which was placed just downstream of the elliptical-shaped leading edge of a 2.9 m long smooth flat plate for the TBL fully developing above the floor of the tunnel. To prevent separation at the leading edge, a length-100mm tailing flap is attached to the trailing edge of the plate, and it was set to about 5° in this study. The maximum approach velocity U_∞ was 8.4 m/s and the corresponding TBL thickness $\delta = 50.8$ mm in the PIV-measured region.

Two kinds of roughness blocks with different resolution levels of six and four, *i.e.*, A6 (the average peak-to-valley roughness height $k_s = 2.34$ mm; the root-mean-square (RMS) roughness height $k_{rms} = 0.64$ mm; the roughness Reynolds number $k_s^+ = k_s u_\tau/\nu = 47$) and A4 ($k_s = 4.01$ mm; $k_{rms} = 0.94$ mm; $k_s^+ = 80$), together with the fully rough (FR) surface ($k_s = 4.2$ mm; $k_{rms} = 1$ mm; $k_s^+ = 84$) and their smooth counterpart (SM, as the baseline surface hereafter) are used to investigate their impacts on the instantaneous energetic large-scale fluctuating turbulent structures in front of and on top of these smooth and roughness-resolved FFSs (*cf.* Figure 1). The four blocks (about 90 × 169 mm^2 for $L \times W$, length × width, $h = 6.35$ mm) were separately placed at the spanwise center of the boundary layer plate at around 2.5 m downstream of the leading edge while other two smooth blocks with the same height (6.35 mm) are placed along their sides to cover the whole width of the wind tunnel test section and thereby form the FFS experimental platform (*cf.* Figure 5 in Wu and Ren [5]. The resulting boundary layer and geometry conditions (*cf.* Table 1) such as Re_h ($= U_\infty h/\nu$, in which ν is the kinematic viscosity) are 3450; $\delta/h = 8$; $L/h = 14.2$ and blockage ratio $h/H = 0.01$. It means that a small blockage ratio but a large δ/h ratio is configured in present work for the TBL developing over the surface transition from a smooth wall to an elevated rough wall since such non-equilibrium boundary layer flows are commonly seen in engineering applications. Moreover, the width aspect ratio (W/h) is 26.6 which are large enough to ensure the qualitative globally two-dimensional behavior of the turbulent flows through a 2D step in theory [3].

Two-dimensional PIV measurements in the x-y plane were conducted at two different spanwise positions, *i.e.*, P1 and P2 in Figure 1 where P1 has a negative roughness slope at the beginning of the FFS top while P2 a positive one.

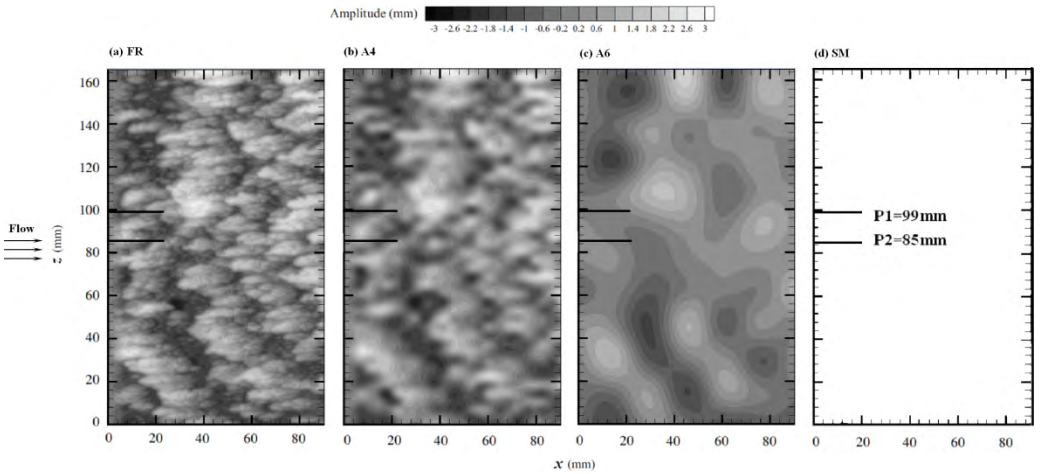

FIGURE 1. The contour plot of fluctuation heights for the roughness-resolved FFS surfaces: (a) the fully rough surface (FR); (b) surface at a resolution level 4 (A4); (c) surface at a resolution level 6 (A6) and (d) the smooth surface step (SM). The two PIV measurement positions are marked with the black lines at P1 = 99 mm and P2 = 85 mm, respectively.

The PIV experimental apparatus parameters and their setup for measurements can be found in Reference [2] and [5]. Measurements were first performed in front of the FFSs, and then the camera was moved downstream to measure the flows on top of the FFSs. The basic TBL flow at $50h$ upstream of the FFSs was also confirmatively measured by PIV to characterize the nature of the approach flow, and its turbulence statistics was not found to be altered due to the presence of the FFSs. The calculated velocity vectors in the dataset to be analyzed have a grid spacing of $h/32$ and the FOV of $5h \times 3.8h$. Each ensemble consists of more than thousand samples of the velocity vector fields for the further statistical study. Their random error in present PIV measurements is approximately 0.1 pixels while the bias errors are estimated to be about 1% of the full-scale velocity since the mean particle image diameter is about 2 pixels.

III. RESULTS AND DISCUSSIONS

A. MEAN VELOCITY

The PIV-measured mean velocity fields in front of and on top of the smooth and roughness-resolved FFSs are presented in Figure 2. Only velocity vectors whose time-averaged streamwise velocity $\langle U \rangle$ are less than $0.5U_\infty$ are shown to highlight the mean separation bubble structures within the recirculation Region I in front of the steps. The other normal uniform flows and the downstream recirculation bubble in Region II on top of the steps are only represented by the streamlines. The red and blue dash-dotted lines mark the locations where the streamwise mean velocity $\langle U \rangle = 0$ and the wall-normal mean velocity $\langle V \rangle = 0$, respectively. Therefore, the locations of the separation and reattachment points, the centers of the bubble structures for the PIV-measured positions at P1 and P2 can be accordingly decided within some certain measurement uncertainties. Ren and Wu [2] and Wu and Ren [5] tabled them and concluded that (I) the mean flow structures in recirculation Region I inclusive the separation and reattachment points, and bubble structure centers for smooth and roughness-resolved FFSs are almost the same, which means that the mean flow in this region is not disturbed by the steps with the different resolution roughness at both positions P1 and P2; however, (II) the flow field of the downstream recirculation Region II is signifycantly distorted by the surface topography of roughness-resolved FFSs and their spanwise position, which was also supported by their statistical results for the mean Reynolds stresses and mean spanwise vorticity as well as the quadrant analysis. Particularly, no clear recirculation bubble structure is observed for the positive-sloped FR and A4 roughness-resolved FFSs at the position P2. Nevertheless, it is worth noting that the effects of the roughness-resolved FFSs on the most energetic and large-scale flow structures in a typical instantaneous velocity field, as previously introduced, are still unknown.

B. POD MODES

An ensemble of 1000 instantaneous fluctuating velocity fields from the dataset was decomposed by the POD method. A platform of the plot (not shown herein for clarity) for the numerical values of the first 10 eigenvalues with different snapshot number (N) of velocity fields show that the POD analysis is fully converged for the 1000 velocity field samples, which means that $N = 1000$ was sufficient enough in minimizing the precision error for POD analysis [19]. The cumulative TKE fractional contributions of the first n POD modes are presented in Table 2. For the flow fields in front of (before) the smooth and roughness-resolved FFSs at P1, the first POD mode accounts for more than 25% of the total energy while the first two modes in sum are almost 40%.

As presented in Wu [18], the large-scale energetic turbulence structures are strongly contributing to the first two eigenmodes. Besides, in this case, the energy of about 90% only contributes from the first 106 modes for SM, 112 for A6,

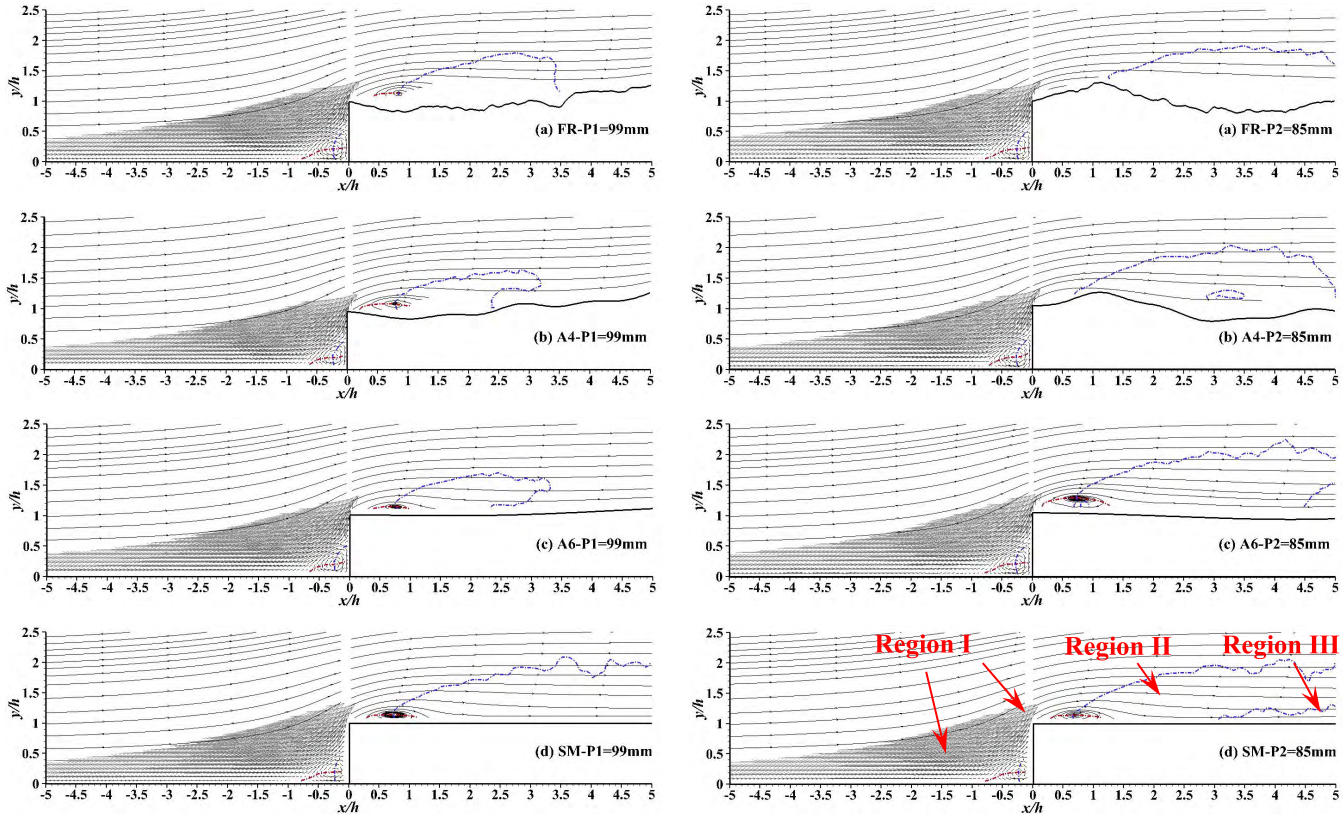

FIGURE 2. Time-averaged turbulent flows over the smooth and roughness-resolved forward-facing step surfaces: (a) FR; (b) A4; (c) A6 and (d)SM at P1 (left) and P2 (right). The red and blue dash-dotted lines mark the locations where streamwise mean velocity $\langle U \rangle = 0$ and wall-normal mean velocity $\langle V \rangle = 0$, respectively. Only those velocity vectors whose $\langle U \rangle < 0.5U_\infty$ are shown to illustrate the mean flow in the recirculation region upstream of the steps while other parts are shown by the streamlines.

110 for A4 and 119 for FR surface, which indicates that the energy contributions from the other larger modes are rather small and we can accordingly reconstruct the flow fields by using the first of approximately 100 low-order modes. Similar energy contributions of POD modes for the flows on top of (over) these FFSs at P1 and P2 are also observed, although in these cases, the contributing energy of the first and the first 2 modes are corresponding about 5∼10 percent less than the ones in front of FFSs cases at P1 and P2. Generally, it can be read from Table 2 that the cumulative TKEs for each mode less than 100 correspondingly decrease till to the first 500 modes when the flows pass through the smooth and roughness-resolved FFSs. The discrepancies of energy contributions for the POD modes between the flows in front of and on top of the steps indicate that the expected significant changes of the energetic large-scale turbulence structures passing over the FFSs. However, these change trends in the cumulative energy are not consistent with that in Iftekhar and Agelin-Chaab [21] where the cumulative TKE increases downstream, which indicates the growth of the large-scale structures. Furthermore, the energy of nearly 90% contributes from the first 166 modes for SM, 162 for A6, 166 for A4 and 154 for FR surface at P1 while, at P2, almost 90% energy is contributing from the first 165 POD modes for SM, 172 for A6, 165 for A4 and 164 for FR, respectively. The reconstructed flows within about 90% energy in front of and on top of these steps are shown hereafter in Figures 11-17.

The fractional energy (*i.e.*, the normalized TKE) distributions of different POD eigenmodes for the fluctuation velocity fields in front of and on top of the smooth and roughness-resolved FFS surfaces are represented in Figure 3. As discussed above, the most TKEs are concentratedly contained within the first few low-order modes and the normalized TKEs in following higher modes decrease dramatically as the eigenmode increases. And interestingly, both TKE spectrums are POD-mode-based fitting to satisfy some kind of scaling law properties with the scaling exponents, −1.1 for relative low-order modes (which is surprisingly very close to the "−1" spectral law in wall-bounded turbulence [22], [23]) given that the influence of steps is considered; and close to the "−1" law of the POD energy spectrum result for our TBL flow data and −2 for the relative high-order ones, respectively. The existence of scaling laws suggests that a possible energy cascade [24] happens among the flow structures, which the low-order/high-order modes represented; and a certain relation between the energy scaling and sub-layer structures, which the measured extremal-point-density has shown [25]. The "−1" power law occurs in

TABLE 2. Cumulative energy (TKE) contributions of the first n POD eigenmodes for the fluctuation velocity fields in front of (before) and on top of (over) the roughness-resolved and smooth FFS surfaces: FR; A4; A6 and SM at P1 and P2.

	Cumulative TKE (%)											
n	Before FFS step at P1				Over FFS step at P1				Over FFS step at P2			
	FR	A4	A6	SM	FR	A4	A6	SM	FR	A4	A6	SM
1	25.33	27.74	27.27	27.45	20.80	20.28	18.92	23.93	19.32	19.10	19.32	19.10
2	36.45	38.43	37.81	38.45	28.66	28.43	28.88	26.31	32.83	30.11	26.87	26.89
3	41.83	43.72	43.41	44.26	32.95	32.58	33.69	31.54	37.50	34.59	31.70	31.96
4	45.85	47.94	47.50	48.26	36.28	36.33	37.56	35.25	40.98	38.10	35.40	35.54
5	49.16	51.37	50.70	54.44	39.26	39.21	40.74	38.50	43.53	41.01	38.77	38.52
20	68.33	70.04	69.67	70.50	61.62	60.37	61.62	60.67	62.36	43.52	60.46	60.70
50	80.57	81.64	81.32	82.09	75.57	74.38	75.24	74.34	75.34	74.93	74.04	74.49
100	88.36	89.14	88.92	89.45	85.05	84.04	84.50	84.03	84.41	84.29	83.65	84.11
106	-	-	-	89.99	-	-	-	-	-	-	-	-
110	-	90.04	-	-	-	-	-	-	-	-	-	-
112	-	-	90.00	-	-	-	-	-	-	-	-	-
119	90.04	-	-	-	-	-	-	-	-	-	-	-
154	-	-	-	-	90.04	-	-	-	-	-	-	-
162	-	-	-	-	-	-	90.01	-	-	-	-	-
164	-	-	-	-	-	-	-	-	90.3	-	-	-
165	-	-	-	-	-	-	-	-	-	90.04	-	89.99
166	-	-	-	-	-	90.00	-	89.98	-	-	-	-
172	-	-	-	-	-	-	-	-	-	-	90.02	-
500	98.64	98.81	98.79	98.83	98.42	98.09	98.12	98.22	98.15	98.17	98.02	98.23
1000	100.0	100.0	100.0	100.0	100.0	100.0	100.0	100.0	100.0	100.0	100.0	100.0

regions of strong TKE production (*cf.* the review table 1 in Reference [26]). In other words, the most energetic large-scale structures are confirmedly characterized by the first lower-order POD modes. And the scaling exponents are not changed with either the different flow conditions in front of/on top of the FFSs or the different FFS roughness surface conditions. In addition, the POD spectrum analysis on the present data indicates again that the flows in front of the smooth and roughness-resolved FFSs are little sensitive to the roughness of FFS surfaces (*cf.* Figure 3(a)), supporting the results regarding the mean velocity patterns discussed in Section III (A). However, the significant effects of the roughness and spanwise positions on the flows over the FFSs can be clearly observed in Figure 3(b), especially for the first ten modes here, which will be hereafter interpreted in Section III (C) from the viewpoint of energetic large-scale structures associated with the first two low-order modes.

The iso-contours of POD mode-shapes for streamwise $\Phi(x)$ and wall-normal $\Phi(y)$ components at the selected first, second, fifth and twentieth mode are illustrated in Figures 4 and 5 for the smooth and three roughness-resolved FFSs at the position P1, respectively. As concluded above, the approaching flows for statistical mean fields in front of the FFSs are almost the same without being affected by the different surface conditions; therefore, only the POD mode-shapes at P1 are given herein for simplicity and clarity. Note that the POD mode-shapes are not actual physical vortex structures or streamline patterns but to be interpreted as the velocity fluctuations which manifest the large-scale patterns of the circulating flow structures [27]; besides, the relative directions of the fluctuating velocity

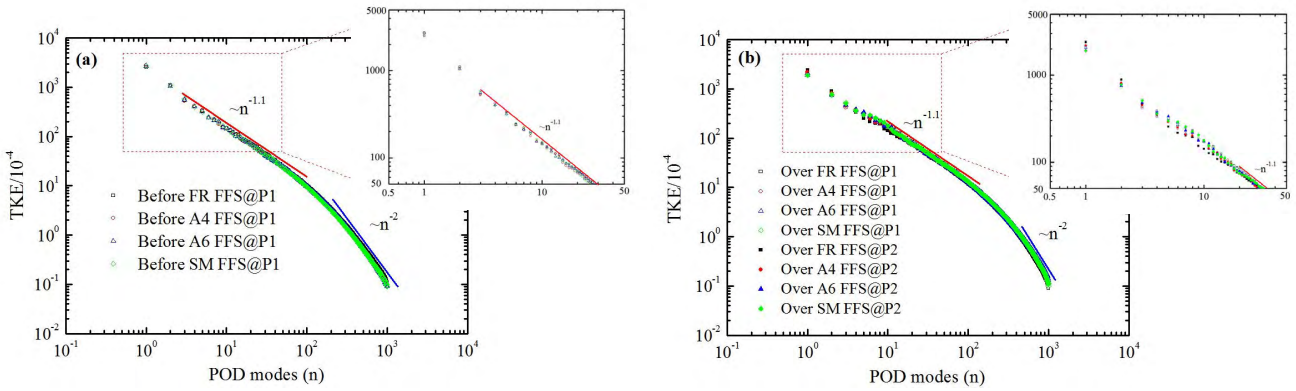

FIGURE 3. Fractional energy (normalized TKE) spectrum distributions of the different *n* POD eigenmodes for the fluctuation velocity fields in front of (before, a) and on top of (over, b) the roughness-resolved and smooth FFS surfaces: FR; A4; A6 and SM at P1and P2.

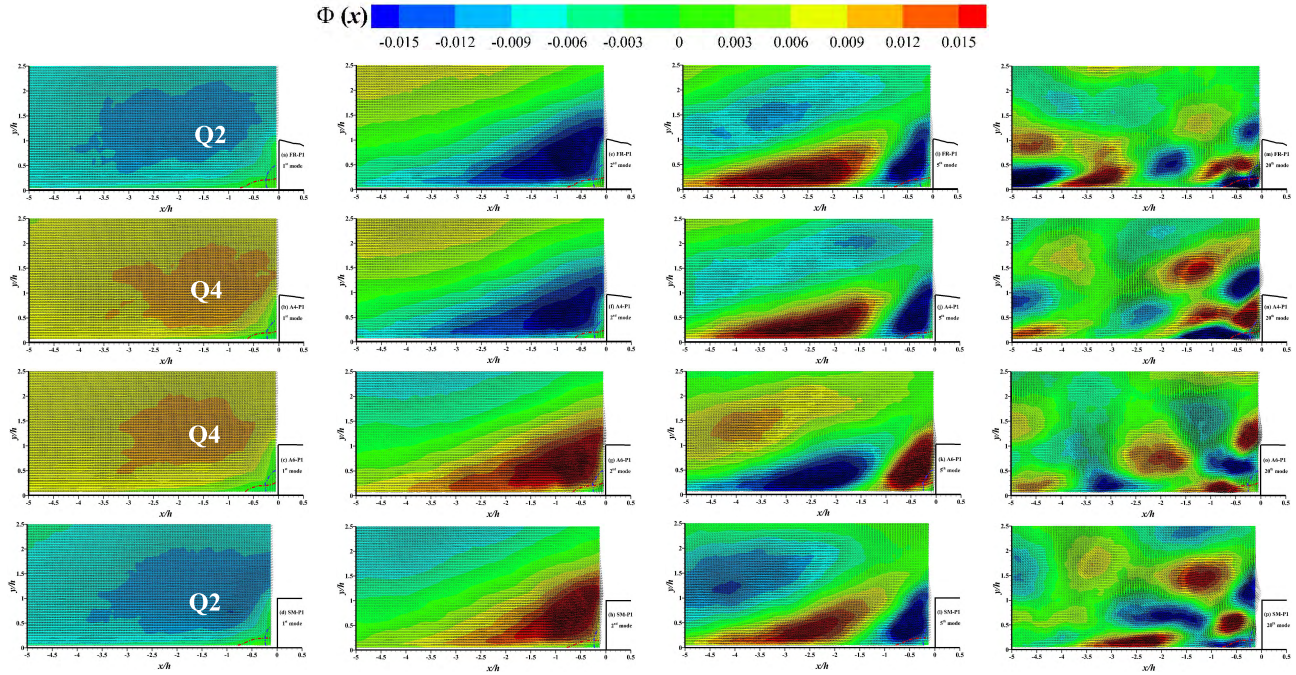

FIGURE 4. Vector patterns and iso-contours corresponding to the *n*-th streamwise POD mode-shapes $\Phi_{n=1,2,5,20}(x)$ in front of the roughness-resolved and smooth FFS surfaces: FR; A4; A6 and SM at P1. Only every second vector resolved is shown for clarity.

fields that the POD mode-shapes represent will change when a POD mode is multiplied with either positive or negative values of its coefficients a_1 [28]. The red and blue dash-dotted lines marking the locations where $\langle U \rangle = 0$ and $\langle V \rangle = 0$ are still shown to roughly represent the mean flow bubble structures at the corner in front of the FFSs. More specifically, the first POD mode, *i.e.*, $\Phi_n = 1$, the most energetic mode as shown in Figures 4 and 5(a-d) respectively, illustrates quite a few large-scale second-quadrant (Q2) or fourth-quadrant (Q4) events which span almost the whole FOV except the corner in front of the steps where the mean bubble structure located. The Reynolds ejection and sweep events with different signs of these velocity fluctuations (Q2: $-u'$, $+v'$; Q4: $+u'$, $-v'$) make the largest contributions to the Reynolds shear stress and the TKE production in wall-bounded turbulence [29]–[31] and they are strongly associated with certain instantaneous flow structures and turbulence intermittent motions. Note that whether Q2 or Q4 events dominating the flow may also be related with the surface roughness conditions of the FFSs and the spanwise locations. And another explanation for this phenomenon observed here is the intrinsic high/low-speed streaks in the approaching TBL flow near the wall and their interaction with the bubbles on the bottom corner in front of the steps [4]. The phenomenon that the most energetic mode illustrating as large-scale Q2 or Q4 events verify that the existence of the large-scale (LS) or very large-scale (VLS) mechanism (although the form that they take is less certain [23]) for

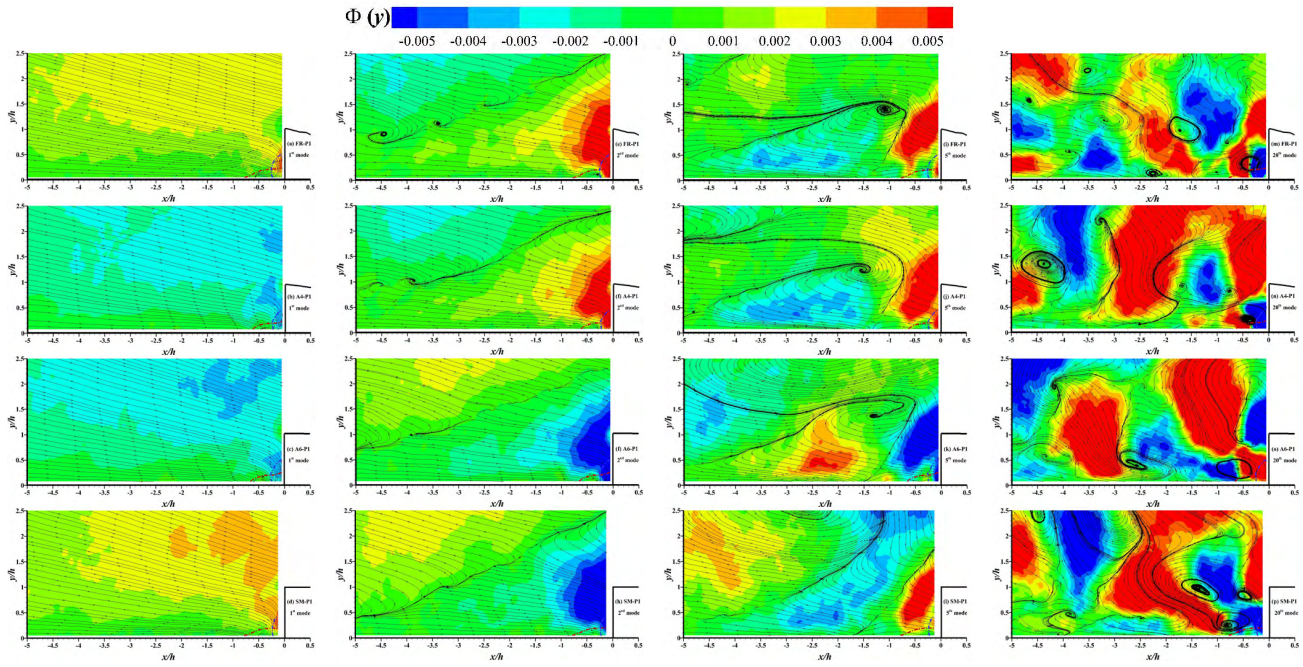

FIGURE 5. Streamline patterns and iso-contours corresponding to the n-th wall-normal POD mode-shapes $\Phi_{n=1,2,5,20}(y)$ in front of the roughness-resolved and smooth FFS surfaces: FR; A4; A6 and SM at P1.

the generation of the approaching wall-bounded turbulent flows and maintaining the turbulence over the FFSs. The LS or VLS motions contribute to almost 30% of the total TKE in the present study. Besides, a long shear layer in the second mode across the whole FOV is illustrated in Figures 4 and 5(e-h), respectively, which presents the interaction of the Reynolds stress events. Interestingly, their inclination angles are changed due to the different roughness conditions of the FFS surfaces, which decrease from 22° to 17° as k_s^+ decreases but increase to 24° for the SM surface. These inclined large-scale structures in the incoming boundary layer illustrated by $\Phi(x)$ in Figure 4 are similar to the conditionally averaged u'-structures which are also visible in Reference [4]. And the strong ejection/sweep events in $\Phi_n = 1$ as well as the shear layer in $\Phi_n = 2$ for the approaching boundary layer are also similarly observed in the classical turbulent boundary layer [18] although the inclination angle of the shear layer here is slightly larger than the case in the zero-pressure gradient TBL flow [32] as a result of the locally adverse pressure gradient due to the presence of the FFSs. For the fifth POD mode $\Phi_n = 5$ shown in Figures 4 and 5(i-l), a clear rotating structure can be observed although the one in Figure 5(l) is not the whole shape due to the limit of the FOV. Note that their wall-normal heights and relative directions of rotation vary from the different roughness surface conditions. The vector and streamline patterns of POD mode-shapes for relative small-scale structures in $\Phi_n = 20$ are separately given in Figures 4 and 5(m-p). No significant changes in sizes or numbers for the contours of $\Phi(x)$ and $\Phi(y)$-POD mode-shapes can be observed. Therefore, we conclude again that, in general, for the statistical flow structures in front of the FFSs, neither the $\Phi(x)$-POD mode-shape nor $\Phi(y)$-POD mode-shape is significantly changed by the different roughness surface conditions. However, the relative rotation direction of flow structures that the streamlines of POD mode-shapes represent appears to be affected by the roughness-resolved FFS surfaces although their common mechanism of the impact from the different surface steps is still an open question, as, for the turbulent flows, the streamlines are unsteady and appear meandering at any instance [4]. Therefore, the typical instantaneous flow fields in which these energetic large-scale structures embedded need to be conditionally captured for interpreting the complex dynamics of the separation region upstream of the smooth and rough-resolved FFSs and for addressing its impacts from the roughness conditions of the FFSs.

Previous studies [2], [5], [6], [15] have reported that the roughness-resolved FFSs had more significant impacts on the statistical mean flow structures on top of the steps than the flows in front of the FFSs. To reveal these impacts, the contours of $\Phi(x)$ and $\Phi(y)$ as well as vector and streamline patterns for the selected first, second, fifth and twentieth-order POD mode-shapes were extracted to show in Figures 6 and 7(a-p) for P1. The region of the recirculation bubble structures and the reattachment point position can be roughly decided by the intersection between the roughness surface and the red or blue dash-dotted lines marking the locations where $\langle U \rangle = 0$ or $\langle V \rangle = 0$, respectively. Note that the flow velocities very close to the top surface cannot

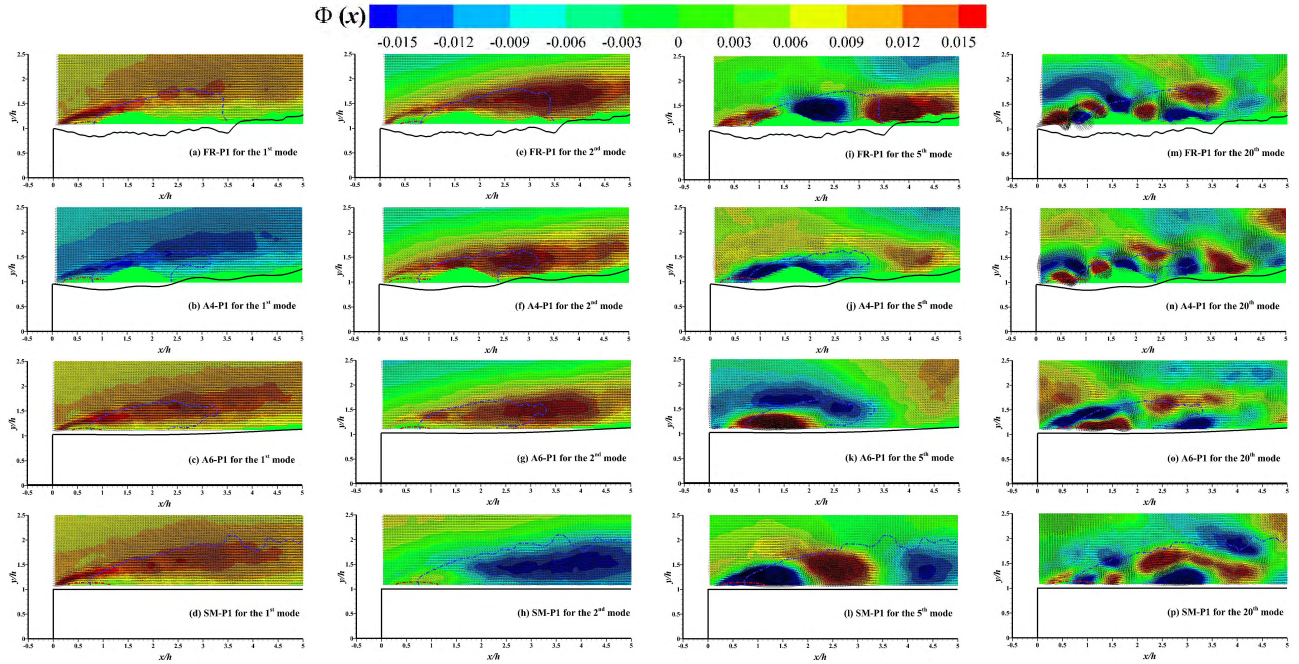

FIGURE 6. Vector patterns and iso-contours corresponding to the n-th streamwise POD mode-shapes $\Phi_{n=1,2,5,20}(x)$ on top of the roughness-resolved and smooth FFS surfaces: FR; A4; A6 and SM at P1. Only every second vector resolved is shown for clarity.

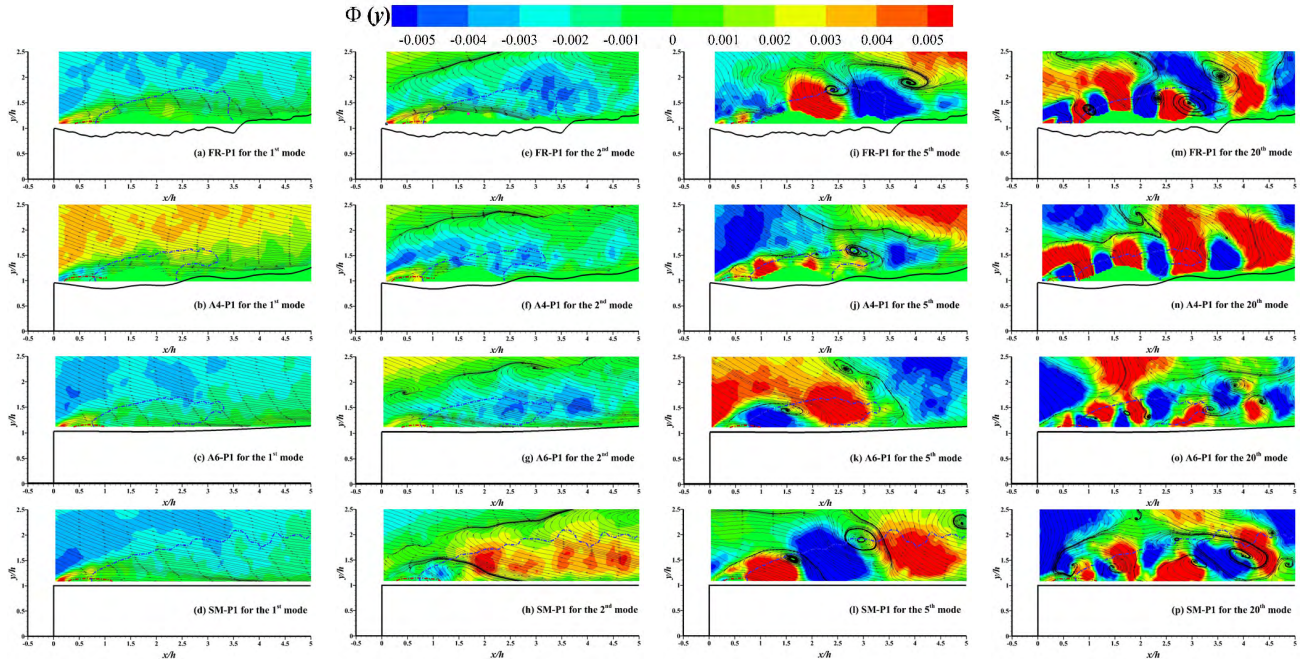

FIGURE 7. Streamline patterns and iso-contours corresponding to the n-th wall-normal POD mode-shapes $\Phi_{n=1,2,5,20}(y)$ on top of the roughness-resolved and smooth FFS surfaces: FR; A4; A6 and SM at P1.

be measured or set to zero herein due to the reflection of laser sheet or the blockage of the higher roughness elements between the laser sheet and camera. Sub-figures (a-d) present the strong Q2 or Q4 events at the field relatively further away from the surface wall in the FOVs. The impacts on the flow from the surface topology conditions mainly happen near the wall for the most energetic structures at the first POD mode. A clear shear layer where the Q2 and Q4 events strongly interacted can be observed as well in the sub-figures (e-h) for the second-order mode. Specifically, these shear layers between the low-speed reverse flow region and the mean free stream flow seem to parallel to the blue dash-dotted line

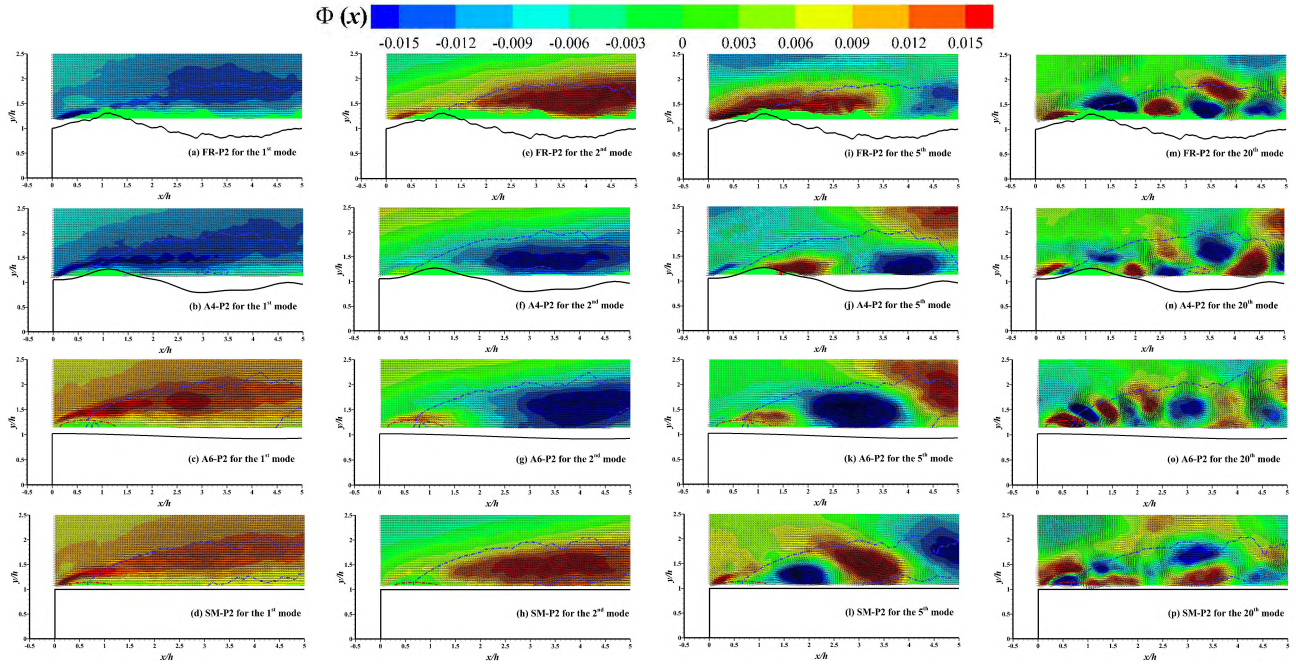

FIGURE 8. Vector patterns and iso-contours corresponding to the *n*-th streamwise POD mode-shapes $\Phi_{n=1,2,5,20}(x)$ on top of the roughness-resolved and smooth FFS surfaces: FR; A4; A6 and SM at P2. Only every second vector resolved is shown for clarity.

where $\langle V \rangle = 0$ at the beginning of flow on top of the steps (*i.e.*, Region II) and their starting position decreases from $y = 1.8h$ to $1.6h$ but the streamwise length increases as the roughness decreases, which means that the shear layers have an outwards-shift trend with the roughness of the wall surfaces increasing. In addition, some secondary structures in small-scale are developing inside the recirculation bubbles which are generated at the upper part of SM surface due to the flow separation at the sharp ledge of the steps; whereas no clear secondary vortices can be seen in other cases. The roughness surfaces suppress the formation of the secondary structures. Similar observations can be found at P2 as shown in Figures 8 and 9(e-h). However, no difference has been seen at this mode for the starting location of shear layers on top of the SM and A6 surfaces although its streamwise length of the SM surface decreases in the FOV at P1 but increases at P2. The flapping trend of the shear layer shifting outwards/ inwards may be related with the fluctuations of the locally adverse pressure when the flows are passing through the steps. Besides, as shown in Figures 8 and 9(i-p), the streamwise and wall-normal mode-shapes both decrease in size but increase in number as the order number of modes increase [15]. Several clockwise rotating or counterclockwise rotating structures are alternately developing along the blue dash-dotted line at fifth and twentieth modes. These structures grow in size downstream along the streamwise direction. This is consistent with the observation at P2. Moreover, we do observe more considerable effects from the different roughness conditions on these flow structures either on their sizes or their numbers. However, no general mechanisms for the impacts from the different surface conditions, such as reduction of the number of recirculating regions; or shortening distances between the recirculating structures and the wall for the increasing roughness surfaces [15], can be observed from the figures due to the three-dimensionality of the roughness surfaces in our cases. It is hard to conclude that these increasing roughness surfaces suppress the vortex formation outside of the recirculation bubble regions based on the given flow information for two positions at P1 and P2. The real energetic large-scale structures contributing more to the TKE or shear stress production in the instantaneous velocity fields need to be conditionally extracted for a further discussion.

Figure 10 shows the histograms of the first two POD coefficients, a_1 and a_2, which is normalized by their corresponding RMS, σ_{a1} and σ_{a2}, respectively; and their Gauss fitting for the velocity fields in front of and on top of the smooth and roughness-resolved FFSs at positions P1 and P2. As presented in the histograms, the first two POD coefficients, a_1 and a_2, are all showing a rough Gaussian distribution whose values are clustered within twice their RMS values except that only a small number of fluctuating velocity fields with a_1 or a_2 are beyond twice of their RMS values. Wu [18] noted that the pattern of symmetric distribution of positive and negative values for a_1 or a_2 indicates that the same contribution from Reynolds ejection (Q2) and sweep (Q4) events to the first two POD modes since the contribution to the first two eigenvalues,*i.e.*, to a part of the TKE, comes from a_1^2 and a_2^2, respectively. Therefore, for these structures or motions in the instantaneous fluctuating velocity fields, the larger positive

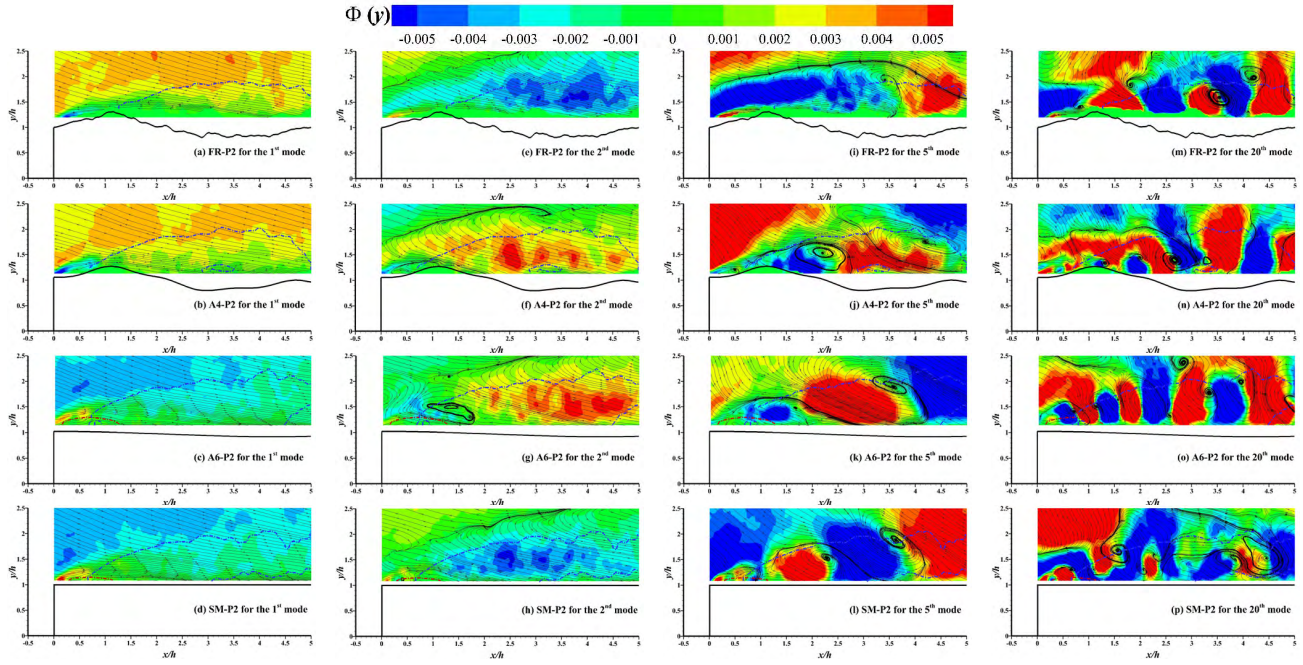

FIGURE 9. Streamline patterns and iso-contours corresponding to the n-th wall-normal POD mode-shapes $\Phi_{n=1,2,5,20}(y)$ on top of the roughness-resolved and smooth FFS surfaces: FR; A4; A6 and SM at P2.

(or negative) value of a_1 (or a_2), the more energetic large-scale structures or the stronger Q2 (Q4) events associated with the first (or second) mode are.

C. INSTANTANEOUS FLUCTUATING VELOCITY FIELD

As previously elaborated, only the instantaneous fluctuating velocity fields containing the most energetic (contributing to a_1, about 8% of the full ensemble velocity fields) and large-scale (to a_2, ∼10%) structures, as well as their POD-based reconstructed fluctuating velocity fields within cumulative 90% TKE are correspondingly analyzed and discussed in this section for the flows in front of and on top of the different roughness FFSs, respectively.

1) ENERGETIC LARGE-SCALE STRUCTURE IN FRONT OF THE FFS$_S$

Figure 11 (or Figure 12) presents several typical instantaneous fluctuation velocity fields with a large positive (or negative) POD coefficient of $a_1 \geq 2\sigma_{a1}$ (or $|a_1| \geq 2\sigma_{a1}$) for the first POD mode in front of the smooth and roughness-resolved FFSs at P1 (left column); and their corresponding reconstructed flows with the TKE of 90% illustrated by the streamlines (right column). The red ($\langle U \rangle = 0$) and blue ($\langle V \rangle = 0$) dash-dotted lines roughly outline the relative locations of time-averaged separation bubble structures. As shown in the figures, irrespective of the surface conditions, the most energetic structures are almost all captured and only the small scale or less energetic structures in the flows (or somewhat PIV measurement errors) has been filtered out, which means that the POD based filter level, 90% of the TKE, is justified to capture the detail information of those large-scale structures. It has been used to reconstruct the classical TBL flows over riblets [33] and, unless specifically stated otherwise, more structural analysis thereafter will focus on the reconstructed flows with this POD-based filter level. As introduced in Section I (A), a typical flow in front of the FFS with a relative high δ/h is, in fact, an oncoming TBL flow and its interaction with the separation bubble structure in Region I. There are two separate forms, *i.e.*, "open" or "closed" type for the flow in this region, as described by Stüer *et al.* [34] and Wilhelm *et al.* [35], which is dependent on whether the fluid is entrained from the outer flow into the bubble or directly by a separation having a focus. Recently, Pearson *et al.* [36] has concluded that the separation bubble in front of the FFS exhibits both open and closed forms with each form behaves for half of the time in the fully TBL flow from their conditional averaging based on the area of reverse flow. More specifically in present study, the most energetic (contributing to a_1) instantaneous structures are present as a large area of Q4 events and several vortex structures when nearly approving the steps with the three-dimensional roughness-resolved surfaces (Figure 11(e-g)) but as a large number of Q2 events and a less few of vortices for the smooth step in Figure 11(h). The separations are now all "open," and there is direct in-plane entrainment of the incoming TBL fluid into the separation region as seen from the streamline patterns although the streamlines of an instantaneous turbulent velocity field are referred as relatively unsteady. Similar flow patterns can be observed in Figure 12 but in which the dominate Reynolds

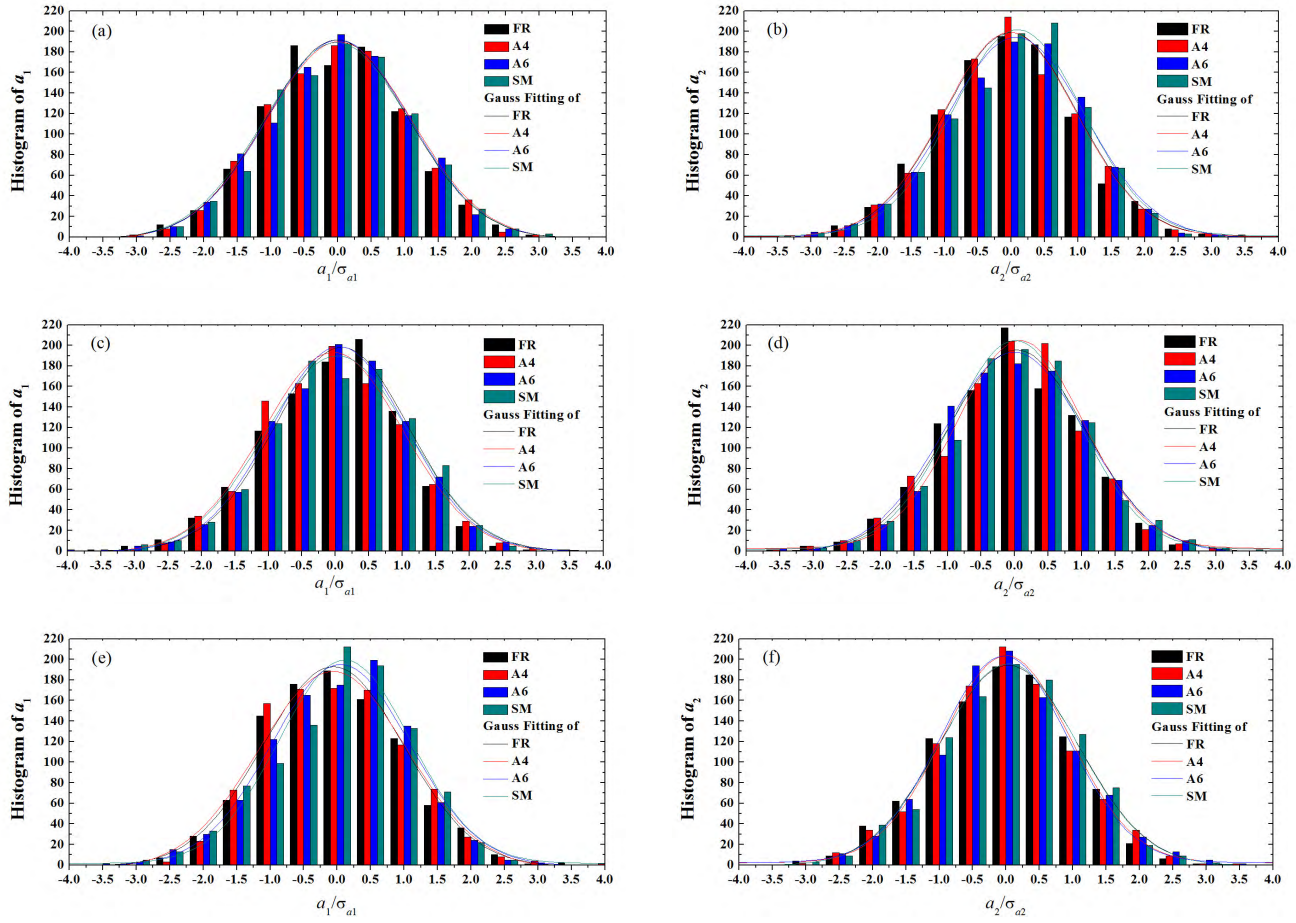

FIGURE 10. Histograms of the first two POD coefficients, (a) a_1 and (b) a_2, normalized by their corresponding RMS (σ_{a1} and σ_{a2}), and their Gauss fitting for the velocity fields in front of the roughness-resolved and smooth FFSs at position P1; (c) a_1 and (d) a_2 for the velocity flows on top of the FFSs at P1; and (e) a_1 and (f) a_2 for the velocity flows on top of these FFSs at P2.

events are changed into Q2 for roughness surfaces, and Q4 events for the smooth step. A closed separation bubble with a focus and a reattachment point on the step face are observed in Figure 12(e) and it is relatively steady and occasionally two-dimensional. This is a direct and instantaneous observation, for the first time, for this form of separation bubble at Region I in front of an FR FFS in the fully TBL although the approaching flow should now be locally three-dimensional enough due to the FR step. Note that all the instantaneous velocity fields with the large POD coefficient of $|a_1| \geq 2\sigma_{a1}$ have these similar flow patterns as shown in Figures 11 and 12, which means that the large-scale Q4 or Q2 events and separation bubbles mostly with an open form are the most energetic instantaneous structures in front of the roughness-resolved FFSs, consistent with the streamwise or wall normal POD mode-shape Φ_1 in Figures 4-5(a-d). And when the surface roughness conditions considered, these most energetic instantaneous flow structures appear to be totally different only between the smooth FFS and its counterpart with roughness due to the local three-dimensionality of the steps. However, the impacts of roughness resolved FFSs on these most energetic instantaneous flow structures here are mainly reflected on the flow above the bubbles, just beyond the height of the step, where the flow becomes less and less local uniform with the increasing k_s^+, especially the flow near the edge of the steps although the roughness has no clear effect on their statistically mean structures [5]. Typical reconstructed flows with the TKE of 90% but with a large POD coefficient of $|a_2| \geq 2\sigma_{a2}$ in front of the FFSs at P1 are presented in Figure 13. The bubble structures can be seen in Region I near the corner in front of the steps and they all behave as open forms for A4, A6 and SM cases, which indicates that they have strong interactions and fluid exchanges with the oncoming TBL flow. However, no clear bubble structure can be observed in Region I for the FR FFS case; and instead, there is a small region of local Q2 events which eject the fluid from the corner. Similarly, irrespective of the surface conditions, the large-scale instantaneous structures shown in Figure 13 behave as a strong shear layer (also *cf.* Figures 4 and 5(e-h)); and near or in which there exists a few strong prograde (nearer the corner) or retrograde (further away from the corner) spanwise vortices and sometimes alternating node and saddle points. We believe that these large-scale instantaneous structures

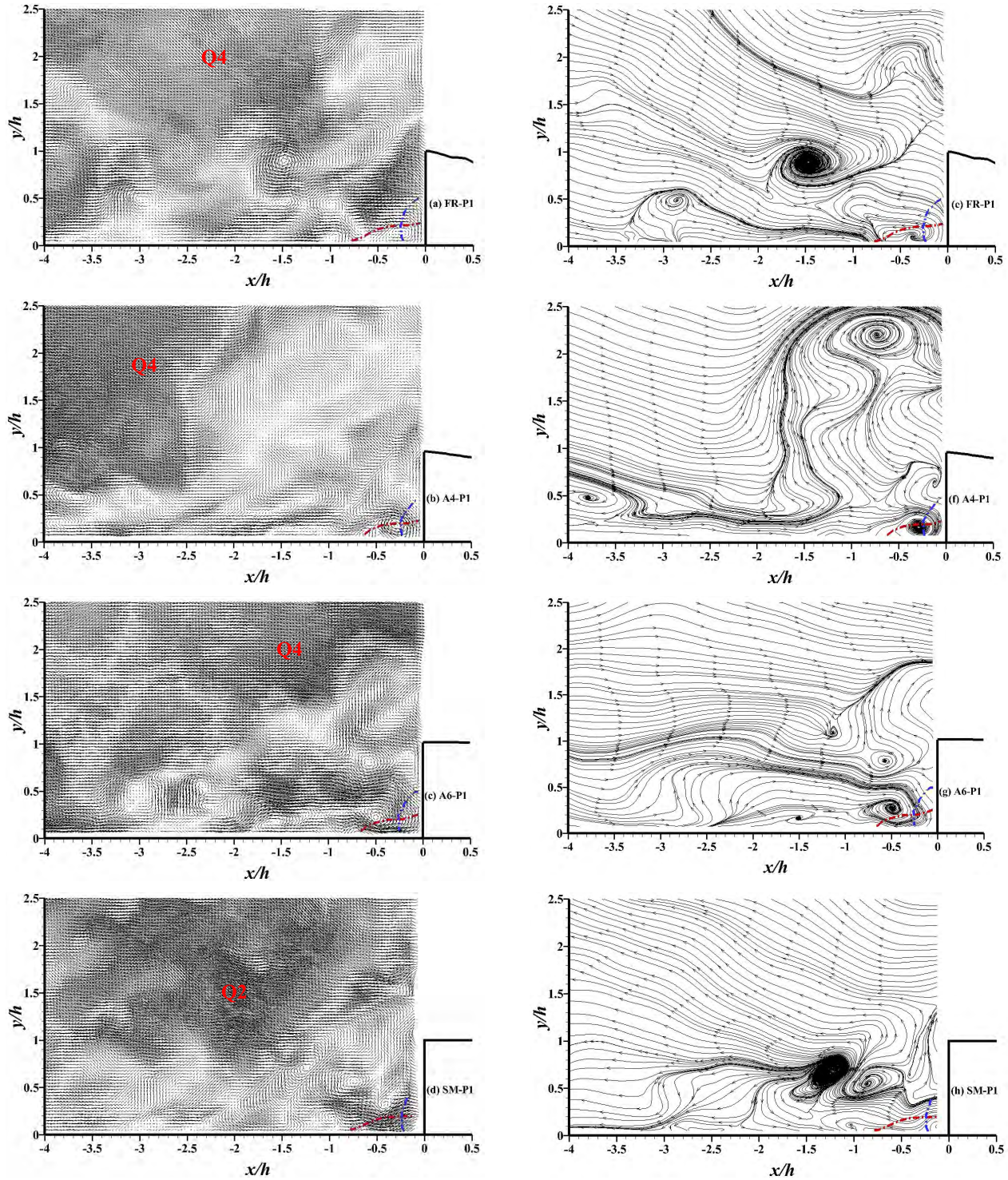

FIGURE 11. Typical instantaneous fluctuating velocity fields in front of the roughness-resolved and smooth FFSs at P1, (a) FR; (b) A4; (c) A6; and (d) SM, with a large positive POD coefficient of $a_1 \geq 2\sigma_{a1}$ for the first POD mode and their corresponding reconstructed flows with the TKE of 90% for the step surfaces of (e) FR; (f) A4; (g) A6; and (h) SM.

(exclusive separation bubbles) are as a result of the interaction between the strong Q4 and Q2 events, similar with the phenomena in the TBL flow [18]. Besides, the presence of the node and saddle points follows that the flow is locally three dimensional and unsteady [3], [4], [34], and it may be related to some kinds of three-dimensional instabilities [34]. No common patterns can be addressed regarding these large-scale structures when the surface conditions are inspected due to the unsteady characteristic of them. However, it is worth summarizing that the leading open form of the separation

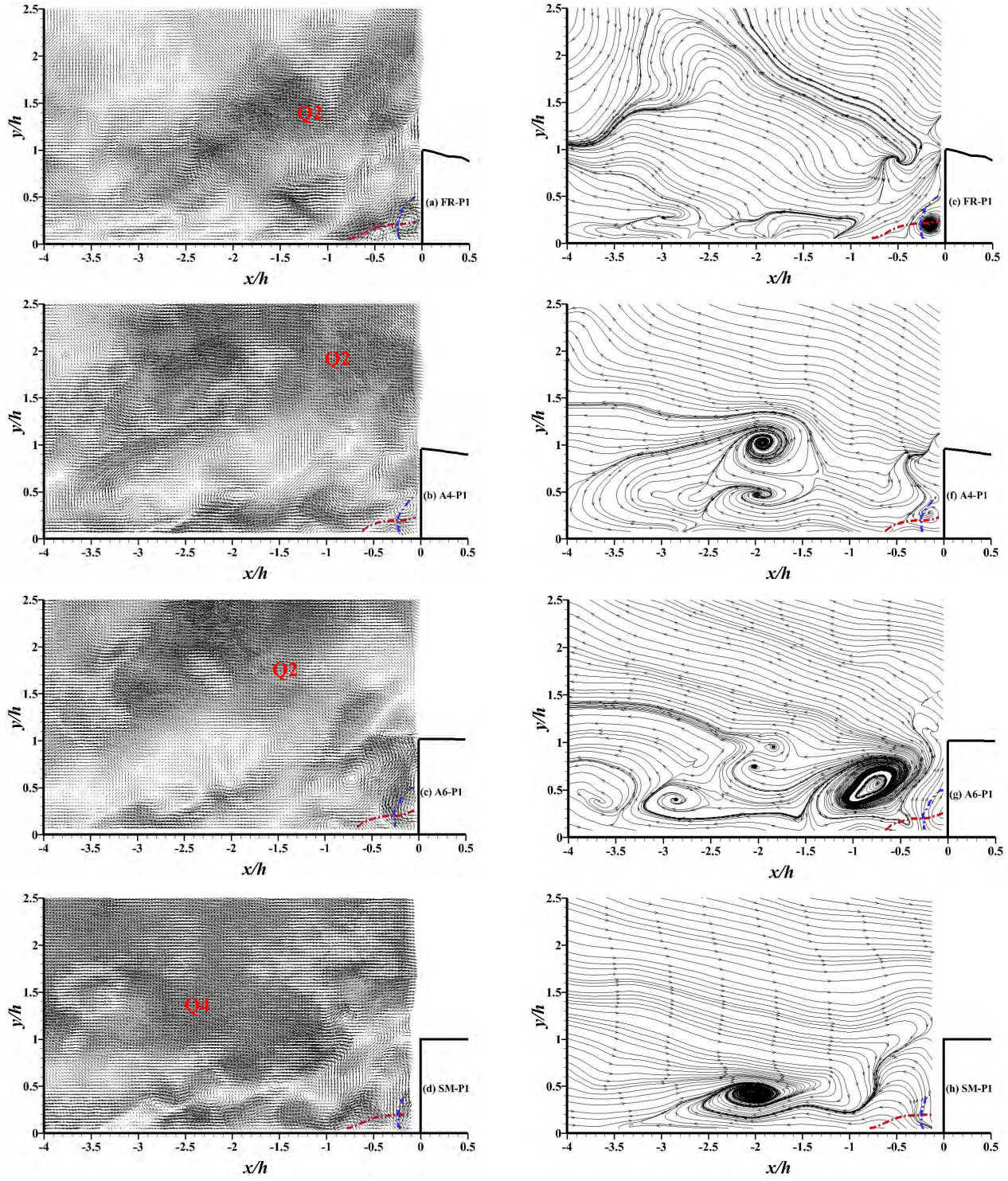

FIGURE 12. Typical instantaneous fluctuating velocity fields in front of the roughness-resolved and smooth FFSs at P1, (a) FR; (b) A4; (c) A6; and (d) SM, with a large negative POD coefficient of $|a_1| \geq 2\sigma_{a1}$ for the first POD mode and their corresponding reconstructed flows with the TKE of 90% for the step surfaces of (e) FR; (f) A4; (g) A6; and (h) SM.

bubble structures in front of less rough FFSs and a small region of local Q2 events at the corner of the FR FFS will be as the first consideration when we want to control these large-scale structures.

2) ENERGETIC LARGE-SCALE STRUCTURE ON TOP OF THE FFS$_S$

As previously introduced in Section I (A), the instantaneous energetic large-scale structures in Regions II and III on top

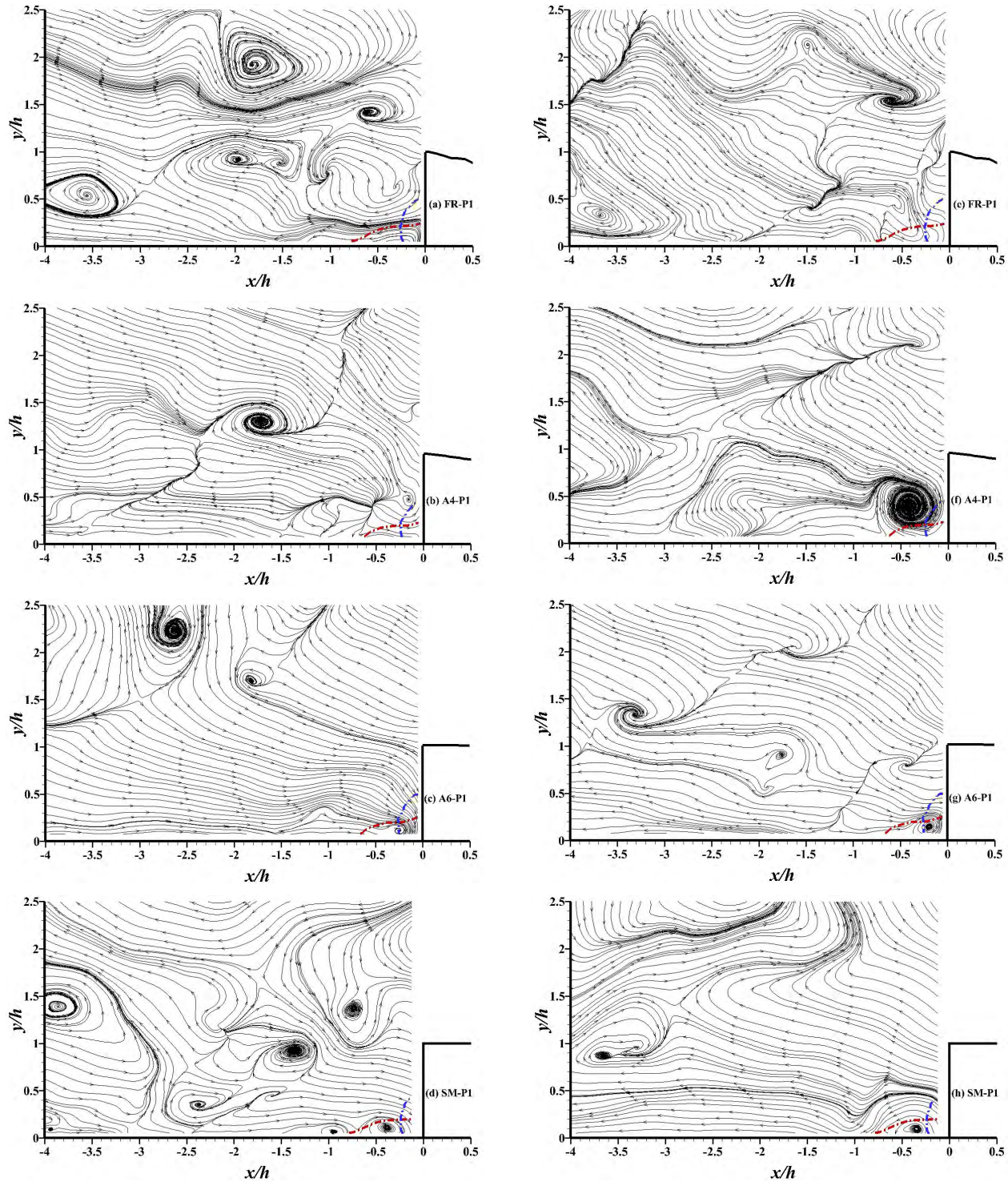

FIGURE 13. Typical reconstructed flows with the TKE of 90% in front of the roughness-resolved and smooth FFSs at P1, (a) FR; (b) A4; (c) A6; and (d) SM, with a large positive POD coefficient of $a_2 \geq 2\sigma_{a_2}$ for the 2nd POD mode and with a large negative POD coefficient of $|a_2| \geq 2\sigma_{a_2}$ for (e) FR; (f) A4; (g) A6; and (h) SM.

of the FFSs, and the impacts of roughness resolution on them will be comparatively discussed in this section based on the past statistical results of [2], [5], and [15]. For the first POD mode with a large temporal coefficient of $|a_1| \geq 2\sigma_{a1}$ typical reconstructed instantaneous fluctuating velocity fields with the TKE of 90% on top of the smooth and roughness-resolved FFSs at P1 are shown in Figure 14. The downstream intersection of red ($\langle U \rangle = 0$) and blue ($\langle V \rangle = 0$)

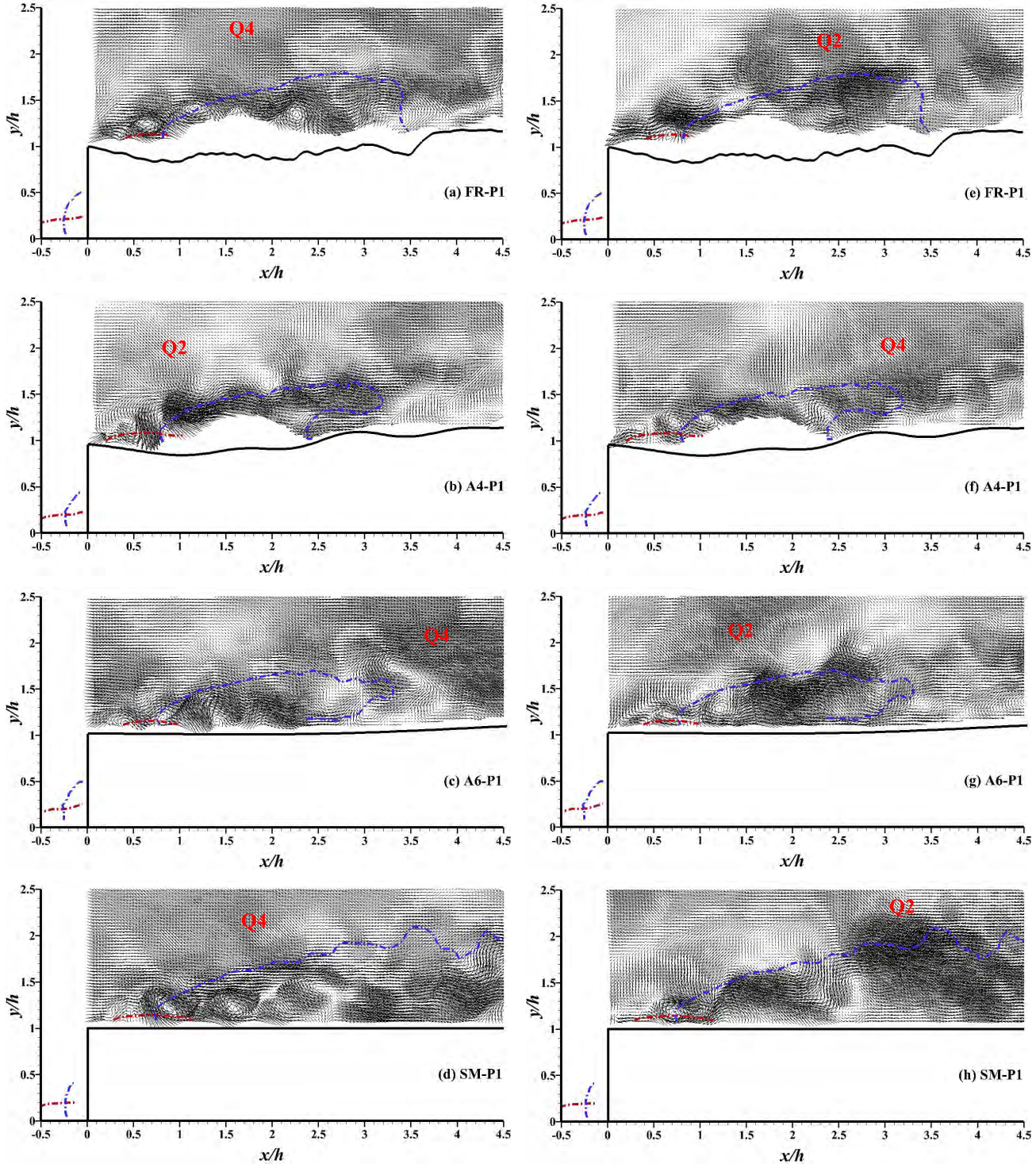

FIGURE 14. Typical reconstructed instantaneous fluctuating velocity fields with the TKE of 90% on top of the roughness-resolved and smooth FFSs at P1, (a) FR; (b) A4; (c) A6; and (d) SM, with a large positive POD coefficient of $a_1 \geq 2\sigma_{a1}$ for the 1st POD mode and with a large negative POD coefficient of $|a_1| \geq 2\sigma_{a_1}$ for (e) FR; (f) A4; (g) A6; and (h) SM.

dash-dotted lines indicate the approximate position of the recirculation bubble center. Similar to the predominant structures in Region I, the most energetic structures present as a great many large-scale Q2 or Q4 events and a few secondary vortex structures at the near-wall. These vortices are almost prograde and rotate in the same sense as the mean shear expect the one in sub-figure (e) (this instantaneous counter clockwise vortex inside the recirculation bubble should be

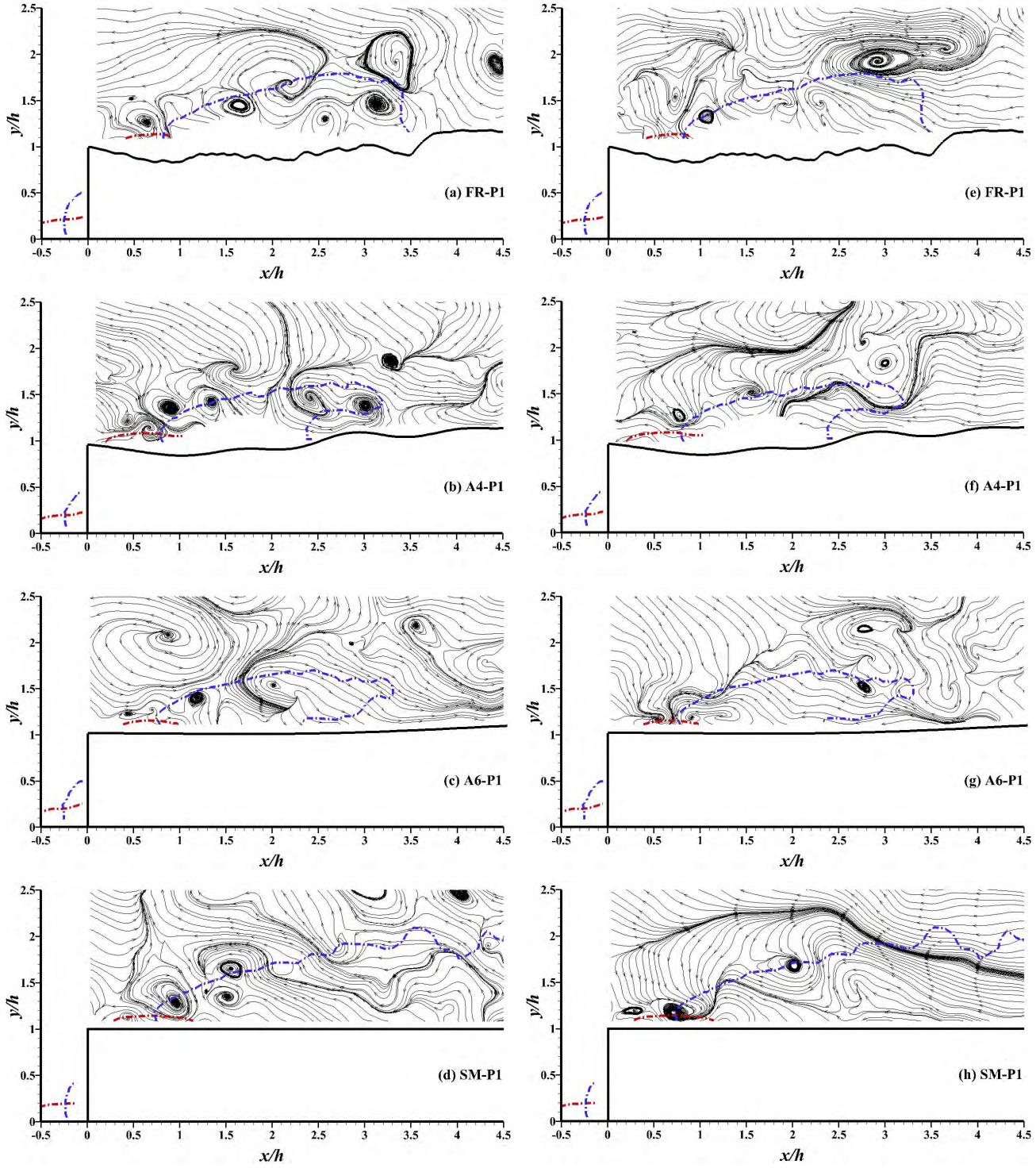

FIGURE 15. Typical reconstructed flows with the TKE of 90% on top of the roughness-resolved and smooth FFSs at P1, (a) FR; (b) A4; (c) A6; and (d) SM, with a large positive POD coefficient of $a_2 \geq 2\sigma_{a2}$ for the 2nd POD mode and with a large negative POD coefficient of $|a_2| \geq 2\sigma_{a2}$ for (e) FR; (f) A4; (g) A6; and (h) SM.

formed due to the local negative roughness slope but favorable pressure gradient). However, the main feature of these large-scale Q4 or Q2 events predominating the flow appears sensitive to the surface roughness conditions as speculated in Section III (B). Specifically, for the FR FFS case, large-scale Q4 events span almost the whole FOV from $x = 0.9h$ to $4.3h$ (sub-figure (a)) while the Q2 events predominate the field from $x = 1.5h$ to $4.5h$ for the large negative

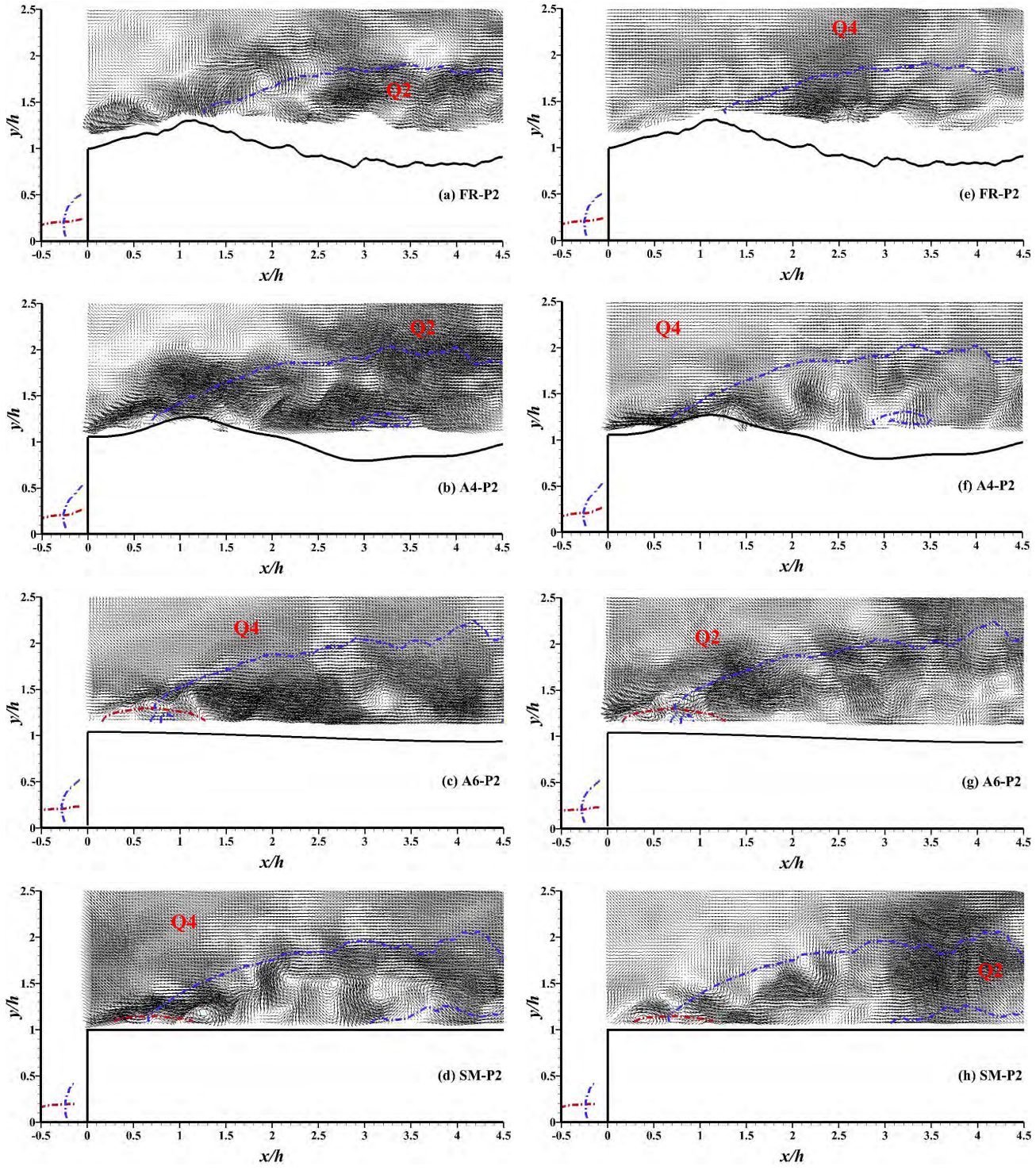

FIGURE 16. Typical reconstructed instantaneous fluctuating velocity fields with the TKE of 90% on top of the roughness-resolved and smooth FFSs at P2, (a) FR; (b) A4; (c) A6; and (d) SM, with a large positive POD coefficient of $a_1 \geq 2\sigma_{a1}$ for the 1st POD mode and with a large negative POD coefficient of $|a_1| \geq 2\sigma_{a_1}$ for (e) FR; (f) A4; (g) A6; and (h) SM.

POD coefficient ((e)). The induced secondary vortex structures observed here are due to the flow shear at near the FR FFS. Similar large-scale turbulent bursting events can be observed for the cases of A6 (see (c), (g)) and SM ((d), (h)) surfaces and their induced vortices grow; shed and then dissipate with distance from the front of the steps. However, for the case of A4 FFS, large-scale Q2 events as shown in sub-figure (b) are the most energetic structures for the large

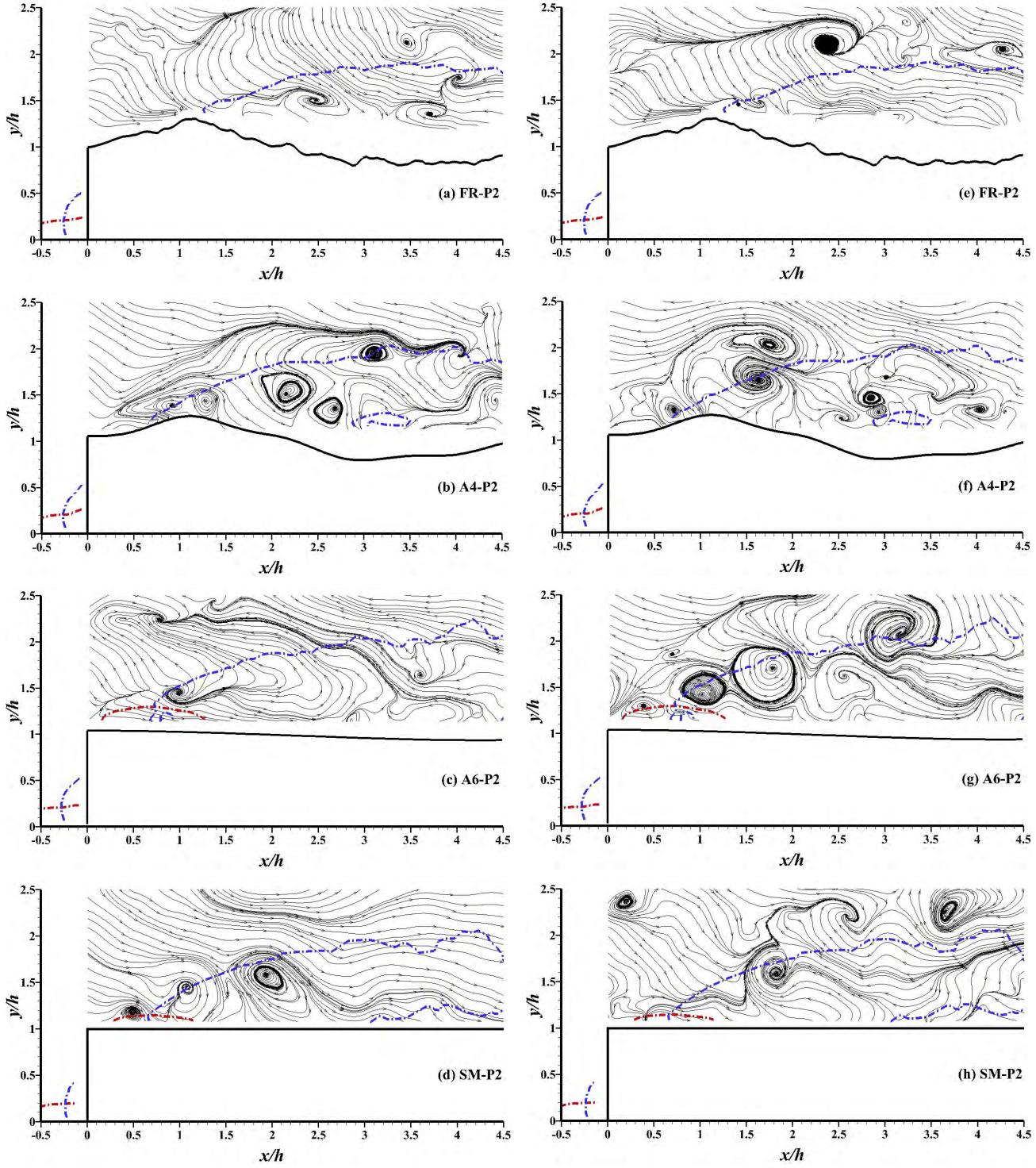

FIGURE 17. Typical reconstructed flows with the TKE of 90% on top of the roughness-resolved and smooth FFSs at P2, (a) FR; (b) A4; (c) A6; and (d) SM, with a large positive POD coefficient of $a_2 \geq 2\sigma_{a2}$ for the 2nd POD mode and with a large negative POD coefficient of $|a_2| \geq 2\sigma_{a2}$ for (e) FR; (f) A4; (g) A6; and (h) SM.

positive POD coefficient while for their negative coefficient of $|a_1| \geq 2\sigma_{a1}$, they are large-scale Q4 events ((f)). Note that we have inspected all the fields one by one which is satisfied the condition of $|a_1| \geq 2\sigma_{a1}$, the main feature of fluctuating velocity fields for each surface condition FFS is similar to the illustration of Figure 14. Therefore, we believe that a step change at the surface due to roughness localizes the disturbance at the wall [37]. In other words, the roughness

impacts on the most energetic structures on top of the steps are local and limited. This can also be seen from Figure 16 where typical reconstructed instantaneous fluctuating velocity fields with 90% TKE on top of the FFSs at P2 are given for smooth and roughness-resolved surfaces. However, the flow patterns at this spanwise position are of significant difference with the one for the surface condition of FR at P1, which are now predominated by the Q2 events for a large positive a_1 and by the Q4 events for a large negative POD coefficient. The more three-dimensional flow for the FR FFS is as a result of the more complicated roughness topology. This means that whether Q2 or Q4 events dominating the flow (regarding the first POD mode) is indeed not only related with the surface roughness conditions of the FFSs but also with the spanwise positions (*cf.* Section III (B)) due to the three-dimensional topology of the roughness surfaces. These observations are different from the POD result of Shao and Agelin-Chaab (2016), which concluded that the step roughness did not affect the first mode, *i.e.*, the most energetic mode. This also inspires us that more careful consideration and a different control scheme need to be given for the three-dimensional roughness-resolved FFS flow. Furthermore, the FR and A4 FFSs modified the series of instantaneous vortex structures which have been observed at P1. Moreover, there is a clear vortex at ($x = 0.7h$, $y = 1.4h$) in Figure 16(a) although the mean bubble structure has disappeared entirely as shown in Figure 2 and [5]; but nothing can be seen in sub-figures (b), (e) and (f) at the front of steps due to the strong positive slope at P2.

Figure 15 and 17 presents that typical reconstructed instantaneous large-scale structures for the flows with a large coefficient of $|a_2| \geq 2\sigma_{a2}$ at P1 and P2, respectively. The large-scale structures observed here overall exhibit as a strong shear layer extending to Region III, under which is the statistically mean bubble (if it did not disappear due to the specific roughness surface); and in which a large number of vortex structures are created, especially for the FR and A4 FFSs at P1. These large-scale vortices, in essence, are different with the ones nearer the wall as seen in Figures 14 and 16, which, in general, have an alternately clockwise and counterclockwise rotation direction along the blue dash-dotted line where $\langle V \rangle = 0$. Largeau and Moriniere [3] concluded that this shear layer and these large-scale structures were generated due to the separation in front of the steps, which plays a vital role in the generation of the wall pressure fluctuations. In addition, for our cases herein, we do find that these large-scale structures are also affected by the roughness-resolved surfaces and spanwise locations, particularly the ones for the SM FFS at P2 where these structures are all prograde. Interestingly, the flow structure pattern without the mean bubble on the front of the steps is different with others, which also hints that we can control the mean bubble to modulate the low-frequency flapping shear layer [3] as well as these large-scale structures.

IV. SUMMARY AND CONCLUSIONS

A new application of the POD method has been performed to mine and analyze the dataset of PIV-measured flow fields in front of and on top of the smooth and roughness-resolved FFSs. The velocity vector fields containing the most energetic large-scale structures are conditionally chosen to show the instantaneous characteristics of this kind of flow. The conditional criterion is that the chosen velocity field whose POD temporal coefficient of the first or second mode is correspondingly larger than twice of their RMS values, *i.e.*, $|a_1| \geq 2\sigma_{a1}$ or $|a_2| \geq 2\sigma_{a2}$, which means that the most TKE has been captured. Besides, the POD filtering function whose filter level is 90% of the TKE has been used to filter out the PIV measurement errors and less energetic small-scale structures in the flows.

The existence of scaling laws in the POD TKE spectrum for the first few relative lower-order modes suggests the energy cascade among the flow structures in front of/on top of smooth and roughness-resolved FFSs. Noticeable roughness impacts on the first few lower-order modes on top of the steps can be observed. The symmetric pattern of Gaussian distribution for positive and negative values of the POD temporal coefficients, a_1 or a_2, indicates that the same contribution from the Reynolds Q2 and Q4 events to the first two POD modes.

In front of the FFSs, the most energetic instantaneous structures are the large-scale Q4 or Q2 events, and the separation bubbles mostly with an open form except only the closed instantaneous one with a focus observed for the first time at Region I before the FR FFS. It is concluded that these most energetic instantaneous structures are very different between the roughness-resolved FFSs and their SM counterpart due to the local three-dimensionality although the mean velocity fields show that there are little roughness impacts on them. The impacts of the resolved roughness on these structures are mainly reflected on the flow above the open bubbles, just beyond the height of the step and at the near-edge where the flow becomes less and less local uniform with k_s^+ increasing. Moreover, the large-scale instantaneous structures behave as a strong shear layer; and near or in which a few prograde or retrograde spanwise vortices; and sometimes, the alternating node and saddle points are existing. The instantaneous patterns are all consistent with the statistical streamwise or wall-normal POD mode-shape Φ_1 and Φ_2. However, no common roughness impacts can be addressed due to the unsteady and three-dimensional characteristic of these large-scale structures. Nevertheless, it is worth summarizing that the leading open form of the separation bubbles before less rough FFSs and a small region of local Q2 events at the corner of the FR FFS will be as the first consideration when the flow control is performed.

Additionally, for the flow on top of the FFSs at P1, the most energetic structures are presented as a great many large-scale Q2 or Q4 events; and a few secondary vortices which are almost prograde at the very near wall and rotate in the same

sense as the mean shear except a counterclockwise one which are inside the recirculation bubble formed due to the local negative roughness slope but a favorable pressure gradient. The main feature of this large-scale Q4 or Q2 events dominating the flow are not only sensitive to the surface roughness conditions although these impacts are local and limited, but to the spanwise locations due to their already local-three-dimensional characteristics, which inspires us that more careful consideration and a different control scheme need to be given when the SM step becomes into three-dimensional roughness-resolved ones. Furthermore, typical instantaneous large-scale structures observed at Region II are overall exhibited as a strong shear layer extending to Region III, under which is the statically mean bubble; and in which a large number of vortex structures are created that in essence are different with the most energetic ones at nearer the wall. The resolved-roughness and spanwise locations affect the large-scale structures, too. Besides, the flow structure pattern without the mean bubble on the front of the steps is distinctly different with others, which also suggests us that the low-frequency flapping shear layer, as well as these large-scale structures, can be modulated using controlling the mean bubble.

REFERENCES

[1] M. Sherry, D. L. Jacono, and J. Sheridan, "An experimental investigation of the recirculation zone formed downstream of a forward facing step," *J. Wind Eng. Ind. Aerodyn.*, vol. 98, no. 12, pp. 888–894, 2010.
[2] H. Ren and Y. Wu, "Turbulent boundary layers over smooth and rough forward-facing steps," *Phys. Fluids*, vol. 23, no. 4, p. 45102, 2011.
[3] J. F. Largeau and V. Moriniere, "Wall pressure fluctuations and topology in separated flows over a forward-facing step," *Exp. Fluids*, vol. 42, no. 1, pp. 21–40, 2007.
[4] D. S. Pearson, P. J. Goulart, and B. Ganapathisubramani, "Turbulent separation upstream of a forward-facing step," *J. Fluid Mech.*, vol. 724, pp. 284–304, Jun. 2013.
[5] Y. Wu and H. Ren, "On the impacts of coarse-scale models of realistic roughness on a forward-facing step turbulent flow," *Int. J. Heat Fluid Flow*, vol. 40, pp. 15–31, Apr. 2013.
[6] S. M. Rifat, A. L. Marchildon, and M. F. Tachie, "Effects of roughness on forward facing step in an open channel," *Int. J. Mech., Aerosp., Ind., Mechtron. Manuf. Eng.*, vol. 10, no. 2, pp. 273–287, 2016.
[7] J. L. Lumley, "The structure of inhomogeneous turbulent flows," in *Atmospheric Turbulence and Radio Wave Propagation*, A. M. Yaglom and V. I. Tatarsky, Eds. Moscow, Russia: Nauka, 1967, pp. 166–178.
[8] G. Berkooz, P. Holmes, and J. L. Lumley, "The proper orthogonal decomposition in the analysis of turbulent flows," *Annu. Rev. Fluid Mech.*, vol. 25, no. 1, pp. 539–575, 1993.
[9] Z. Tang and N. Jiang, "Dynamic mode decomposition of hairpin vortices generated by a hemisphere protuberance," *Sci. China Phys., Mech. Astron.*, vol. 55, no. 1, pp. 118–124, 2012.
[10] L.-H. Feng, J.-J. Wang, and C. Pan, "Proper orthogonal decomposition analysis of vortex dynamics of a circular cylinder under synthetic jet control," *Phys. Fluids*, vol. 23, no. 1, p. 014106, 2011.
[11] Q. Zhang, Y. Liu, and S. Wang, "The identification of coherent structures using proper orthogonal decomposition and dynamic mode decomposition," *J. Fluids Struct.*, vol. 49, pp. 53–72, Aug. 2014.
[12] Q. Zhang and Y. Liu, "Influence of incident vortex street on separated flow around a finite blunt plate: PIV measurement and POD analysis," *J. Fluid Struct.*, vol. 55, pp. 463–483, May 2015.
[13] R. J. Adrian, K. T. Christensen, and Z.-C. Liu, "Analysis and interpretation of instantaneous turbulent velocity fields," *Exp. Fluids*, vol. 29, no. 3, pp. 275–290, 2000.
[14] H. Wang, Q. Gao, L. Feng, R. Wei, and J. Wang, "Proper orthogonal decomposition based outlier correction for PIV data," *Exp. Fluids*, vol. 56, no. 2, p. 43, 2015.
[15] W. Shao and M. Agelin-Chaab, "Turbulent flows over forward facing steps with surface roughness," *J. Fluids Eng.*, vol. 138, no. 2, p. 21103, 2016.
[16] L. Namgyal and J. W. Hall, "Coherent streamwise vortex structures in the near-field of the three-dimensional wall jet," *J. Fluids Eng.*, vol. 135, no. 6, p. 61204, 2013.
[17] L. Sirovich, "Turbulence and the dynamics of coherent structures. Part I: Coherent structures," *Quart. Appl. Math.*, vol. 45, no. 3, pp. 561–571, 1987.
[18] Y. Wu, "A study of energetic large-scale structures in turbulent boundary layer," *Phys. Fluids*, vol. 26, no. 4, p. 045113, 2014.
[19] Y. Wu *et al.*, "Proper-orthogonal-decomposition study of turbulent near wake of S805 airfoil in deep stall," *AIAA J.*, vol. 55, no. 6, pp. 1959–1969, 2017.
[20] H. Chen, D. L. Reuss, and V. Sick, "On the use and interpretation of proper orthogonal decomposition of in-cylinder engine flows," *Meas. Sci. Technol.*, vol. 23, no. 8, p. 85302, 2012.
[21] H. Iftekhar and M. Agelin-Chaab, "Structure of turbulent flows over forward facing steps with adverse pressure gradient," *J. Fluids Eng.*, vol. 138, no. 11, p. 111202, 2016.
[22] V. Nikora, "Origin of the '−1' spectral law in wall-bounded turbulence," *Phys. Rev. Lett.*, vol. 83, no. 4, p. 734, 1999.
[23] B. J. Balakumar and R. J. Adrian, "Large- and very-large-scale motions in channel and boundary-layer flows," *Philos. Trans. Roy. Soc. A, Math., Phys. Eng. Sci.*, vol. 365, no. 1852, pp. 665–681, 2007.
[24] J. Jiménez, "Cascades in wall-bounded turbulence," *Annu. Rev. Fluid Mech.*, vol. 44, no. 1, pp. 27–45, 2011.
[25] Y. Huang, L. Wang, F. G. Schmitt, X. Zheng, N. Jiang, and Y. Liu, "Extremal-point density of scaling processes: From fractional Brownian motion to turbulence in one dimension," *Phys. Rev. E, Stat. Phys. Plasmas Fluids Relat. Interdiscip. Top.*, vol. 96, p. 012215, Jul. 2017.
[26] G. Katul and C.-R. Chu, "A theoretical and experimental investigation of energy-containing scales in the dynamic sublayer of boundary-layer flows," *Boundary-Layer Meteorol.*, vol. 86, no. 2, pp. 279–312, 1998.
[27] B. W. van Oudheusden, F. Scarano, N. P. van Hinsberg, and D. W. Watt, "Phase-resolved characterization of vortex shedding in the near wake of a square-section cylinder at incidence," *Exp. Fluids*, vol. 39, no. 1, pp. 86–98, 2005.
[28] S. Munir, M. I. Siddiqui, M. Heikal, A. R. A. Aziz, and G. de Sercey, "Identification of dominant structures and their flow dynamics in the turbulent two-phase flow using POD technique," *J. Mech. Sci. Technol.*, vol. 29, no. 11, pp. 4701–4710, 2015.
[29] Z.-Q. Tang, N. Jiang, A. Schröder, and R. Geisler, "Tomographic PIV investigation of coherent structures in a turbulent boundary layer flow," *Acta Mech. Sinica*, vol. 28, no. 3, pp. 572–582, 2012.
[30] S. Yang and N. Jiang, "Tomographic TR-PIV measurement of coherent structure spatial topology utilizing an improved quadrant splitting method," *Sci. China Phys., Mech. Astron.*, vol. 55, no. 10, pp. 1863–1872, 2012.
[31] J. M. Wallace, "Quadrant analysis in turbulence research: History and evolution," *Annu. Rev. Fluid Mech.*, vol. 48, pp. 131–158, Jan. 2016.
[32] R. J. Adrian, C. D. Meinhart, and C. D. Tomkins, "Vortex organization in the outer region of the turbulent boundary layer," *J. Fluid Mech.*, vol. 422, pp. 1–54, Nov. 2000.
[33] S. Li, N. Jiang, S. Yang, Y. Huang, and Y. Wu, "Coherent structures over riblets in turbulent boundary layer studied by combining time-resolved particle image velocimetry (TRPIV), proper orthogonal decomposition (POD), and finite-time Lyapunov exponent (FTLE)," *Chin. Phys. B*, vol. 27, no. 10, p. 104701, 2018.
[34] H. Stüer, A. Gyr, and W. Kinzelbach, "Laminar separation on a forward facing step," *Eur. J. Mech.-B/Fluids*, vol. 18, no. 4, pp. 675–692, 1999.
[35] D. Wilhelm, C. Härtel, and L. Kleiser, "Computational analysis of the two-dimensional–three-dimensional transition in forward-facing step flow," *J. Fluid Mech.*, vol. 489, pp. 1–27, Jul. 2003.
[36] D. S. Pearson, P. J. Goulart, and B. Ganapathisubramani, "Investigation of turbulent separation in a forward-facing step flow," *J. Phys., Conf. Ser.*, vol. 318, no. 2, p. 22031, 2011.
[37] A. J. Smits and D. H. Wood, "The response of turbulent boundary layers to sudden perturbations," *Annu. Rev. Fluid Mech.*, vol. 17, no. 1, pp. 321–358, 1985.

YANG SHAOQIONG is currently a Lecturer and the Master's Tutor with the School of Mechanical Engineering, Tianjin University. His research interests include the experimental fluid mechanics on flow control for turbulence and the hydrodynamic shape optimization for autonomous underwater vehicle/glider and their drag reduction strategies.

He received the combined master's and Ph.D. degrees in engineering from the Department of Mechanics, School of Mechanical Engineering, Tianjin University.

He studied for one year at the University of Nottingham, U.K., from 2013 to 2014, under the supervision of Prof. K.-S. Choi. He was with Nanyang Technological University, Singapore, as a Research Fellow, from 2015 to 2017. Since 2017, he has been with the Underwater Robot Team, School of Mechanical Engineering, Tianjin University. He was a recipient of the Ministry of Education Academic Newcomer Award, China, in 2012.

WANG YANHUI received the B.S., M.S., and Ph.D. degrees in mechanical engineering from Tianjin University. He is currently the Ph.D. graduates' Supervisor. He is also the Deputy Director of the Marine Equipment Technology Engineering Center of Tianjin and also the Director of the Marine Observation Branch of Chinese Oceanology and Limnology Institute. He was a recipient of the National Excellent Youth Fund Winner, Young Scholar of the Yangtze River of the Ministry of Education, and Tianjin Young and Middle-aged Scientific and Technological Innovation Leading Talent in China. He is the Editorial Board Member of the *Journal of Underwater Unmanned Systems* and a member of the Institute of IEEE Robotics and Automation.

In recent years, he has taken charge of more than ten scientific projects, including the National Natural Science Foundation of China, the National Key R&D Program of China, and the National High-tech R&D Program of China (863 Program). Towards underwater equipment performance requirements of deep diving, long duration, and high precision, he focuses his systematic research both on fundamental theories and technical implementation.

Some of his achievements, like the underwater glider, Petrel, and so on, have been listed in China's Top Ten Ocean Scientific and Technological Advances for, 2015. He was also a recipient of the first prize of Tianjin Technological Invention Award, for 2015, the second prize of the National Technical Inventions Award, for 2016, and a Chinese Patent Award of Excellence. Journals like *Popular Science* and *Armada International* in the U.S. have commented that Petrel is the first glider of China, and that Petrel creates Chinese glider records of the voyage, depth, and endurance.

YANG MING received the B.S. degree in mechanical engineering from Tianjin University, where he is currently pursuing the Ph.D. degree in mechanical engineering with the School of Mechanical Engineering. His research interests include overall design, motion parameters optimization, and drag-reduction strategies for underwater gliders.

SONG YANG received the B.S. degree in mechanical engineering from Tianjin Polytechnic University, in 2014, and the M.S. degree in mechanical engineering from Tianjin University, in 2017, where he is currently pursuing the Ph.D. degree in mechanical engineering with the School of Mechanical Engineering. His research interests include developing buoyancy driving systems and the energy management strategy for underwater gliders.

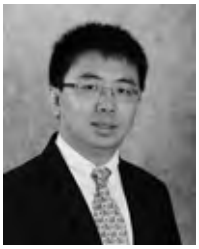

WU YANHUA received the B.Eng. degree in engineering thermo-physics and the B.A. degree in English in science and technology from Tianjin University, China, in 1997, the M.S. degree in mechanical engineering from The University of New Mexico, in 2004, and the Ph.D. degree in theoretical and applied mechanics from the University of Illinois at Urbana–Champaign, in 2008. He was a Thermal Control Engineer for satellites with the Beijing Institute of Spacecraft System Engineering, Beijing, China, until 2001.

He joined the School of Mechanical and Aerospace Engineering, in 2011. He was an Assistant Professor with the Department of Mechanical and Materials Engineering, Wright State University, Dayton, OH, USA, before joining NTU. He is a Senior Member of the American Institute of Aeronautics and Astronautics, and a member of the American Society of Mechanical Engineering and the American Physical Society.